Received: 12 February 2025 | Revised: 13 May 2025 | Accepted: 16 September 2025

DOI: 10.1002/qj.70049

Quarterly Journal of the Royal Meteorological Society RMetS

RESEARCH ARTICLE

When tiny convective spread affects a midlatitude jet: Spread sequence

Edward Groot[1,2] | **Michael Riemer**[2]

[1]Atmospheric, Oceanic and Planetary Physics, University of Oxford, UK

[2]Institut für Physik der Atmosphäre, Johannes Gutenberg University, Mainz, Germany

Correspondence
Edward Groot, Atmospheric, Oceanic and Planetary Physics, University of Oxford, UK.
Email: large.edward.simulations@gmail.com

Funding information
Leverhulme Trust grant funds EG's current position at the University of Oxford. In addition, both authors acknowledge TRR-165 'WavestoWeather' by the German Research Foundation (DFG), Grant/Award Number: RPG-2022-192

Abstract

We investigate the spread evolution over 3 days in an ensemble experiment starting from tiny initial condition uncertainty. We simulate a real event during which three mesoscale convective systems occur in close proximity to the midlatitude jet. Combining ensemble sensitivity analysis with a spread-growth diagnostic based on piecewise potential-vorticity tendencies, we compare the spread evolution with an existing conceptual three-stage model. Each system follows the first stage, characterised by development of convective variability. Nevertheless, we find significant variation among the systems in their propensity to interact with the jet stream, which characterises the second conceptual stage. One exemplary convective system follows the conceptual evolution of Baumgart et al.: convective uncertainty initially projects onto the jet by upper tropospheric outflow, which further amplifies spread through balanced nonlinear growth as it propagates downstream. Rossby-like dispersion in the downstream spread is strongly associated with the convective variability. In contrast, for another convective system, convective variability projects onto the local anticyclonic flow aloft only. Subsequently, this anticyclonic perturbation does not project considerable convective uncertainty onto the straight jet stream, which truncates the conceptual spread evolution. For the third system, negligible fingerprints of distinct spread-growth stages (beyond the initial stage) are identified. Alongside convective heating, long-wave radiation jointly dominates the spread evolution near the convective systems, whereas earlier studies suggest convective heating by the deep-convective parametrisation dominates. Long-wave radiative tendencies of convective anvils outlive the accompanied heating tendencies and extend spatially. Furthermore, we link convective variability of the exemplary system directly to long-wave radiative tendencies. Therefore, long-wave radiation appears to contribute substantially to stages 1 and 2 here. Finally, we identify flow dependence of the impact of convection on the jet, which may relate to the wave-relative location of convective systems. Hence, we advocate to improve understanding of particularly favourable conditions for downstream propagation of convective variability.

KEYWORDS

spread growth, spread sequence, jet stream, interaction, mesoscale convective system, convective uncertainty, flow dependence, Rossby dispersion, convective heating, long-wave radiative heating, conditional predictability, intrinsic predictability, intrinsic limit, spread decomposition divergent, rotational

1 | INTRODUCTION

Atmospheric predictability is ultimately limited by the butterfly effect (Lorenz, 1969; Palmer *et al.*, 2014); that is, the rapid growth of forecast spread at small scale and its impact on successively increasing scales. Current-day operational forecasts have not yet reached this limit (e.g., Judt, 2018; Selz, 2019; Selz *et al.*, 2022; Zhang *et al.*, 2019), and a better understanding of the "butterfly effect" helps to assess the remaining improvement potential. The seminal work by Lorenz (1969) describes this upscale spread growth in terms of a two-dimensional model, in which scale interactions are described as if the atmosphere were fully developed two-dimensional turbulence (with continuous upscale and downscale interaction). This model thereby assumes self-similarity across scales, implying that the underlying spread-growth mechanism is independent of scale. More recent work, however, identified that moist convection, which is unrepresented in Lorenz's model, is of crucial importance for rapid spread growth at small scales (e.g., Hohenegger & Schar, 2007; Selz & Craig, 2015; Zhang *et al.*, 2007).

Moving beyond Lorenz's assumption of self-similarity of spread growth, Zhang *et al.* (2007) introduced a three-stage conceptual model with each stage being dominated by distinct growth mechanisms. Baumgart *et al.* (2019) analysed spread-growth mechanisms quantitatively and confirmed a three-stage sequence of upscale spread growth, but with some differences in the interpretation of the dominant spread-growth mechanisms. Baumgart *et al.*'s quantification of spread-growth mechanisms is based on the potential vorticity (PV) perspective of forecast spread (Davies & Didone, 2013). From this PV perspective, the pattern of forecast errors, or forecast spread, in the midlatitudes is dominated by the PV errors in the tropopause region. A distinct advantage of a PV perspective is that standard piecewise PV thinking for midlatitude dynamics (e.g., Davis *et al.*, 1996; Teubler & Riemer, 2021) can be applied to identify individual spread-growth mechanisms (Baumgart *et al.*, 2018, 2019; Baumgart & Riemer, 2019; Binder *et al.*, 2021; Selz *et al.*, 2022). In addition, the approach has proven useful to yield insight into differences in the dynamical evolution that arise from differences in the representation of physical processes (specifically demonstrated for cloud-radiative impacts on idealised cyclones; Keshtgar *et al.*, 2023).

The three-stage sequence of spread growth in Baumgart *et al.* (2019) has been identified in the mean behaviour of a number of spread-growth experiments (distributed evenly over a year) when averaged over large domains. From this mean perspective, spread growth is initially (in the first 12 hr) dominated by the stochastic (deep) convection scheme, in the subsequent 36 hr by upper tropospheric divergent flow, and finally by the rotational (non-divergent) flow. This picture holds for initial condition uncertainty with very small amplitude. Increasing initial condition uncertainty, a transition in the relative importance of spread-growth mechanisms is observed (Selz *et al.*, 2022). For current-day initial condition uncertainty, spread growth at initial time is on average already dominated by the rotational wind. This transition in the relative importance of spread-growth mechanisms provides further evidence for the idea that the intrinsic limit of predictability is indeed characterised by the three-stage sequence of spread growth (Selz *et al.*, 2022). The dominance of the convection scheme during the first stage is consistent with earlier notions of the importance of latent heat release in convection for rapid small-scale spread growth when convection is resolved (Hohenegger & Schar, 2007; Selz & Craig, 2015; Zhang *et al.*, 2007). The progression to divergent winds as mediator during the second stage is consistent with the idea that a general adjustment-to-balance-process projects spread from precipitation regions to larger scales: differences in latent heat release lead to differences in the divergent component of the wind and in the subsequent (geostrophically) balanced state on the inertial time-scale of approximately 12 hr (Bierdel *et al.*, 2017, 2018; Selz & Craig, 2015; Zhang *et al.*, 2007). Baumgart *et al.* (2019), however, hypothesise a more effective principal pathway for the divergent winds to project spread upscale: that differences in the divergent, convective outflow lead to differences in displacements of the sharp PV gradient associated with the midlatitude jet, and thus to large-amplitude, meso-scale PV spread. In the third stage, this spread grows further by quasi-barotropic nonlinear interaction (Baumgart *et al.*, 2018, 2019), consistent with the spread-growth mechanism in the Lorenz (1969) model.

The mean perspective on spread growth provided by Baumgart *et al.* (2019) and Selz *et al.* (2022) suggests an intriguing picture: variability in latent heat release in convective systems generates variability in the upper tropospheric divergent winds, which directly project variability onto the large PV gradient associated with the jet stream. The sensitivity of upper tropospheric PV above convective systems and the subsequent evolution of the downstream flow to the representation of convective systems is well known (e.g., Clarke *et al.*, 2019a, 2019b; Done *et al.*, 2006; Lojko *et al.*, 2022; Rodwell *et al.*, 2013). Furthermore, mesoscale convection is known to create PV dipole patterns with negative anomalies downshear and above heating anomalies (e.g., Chagnon & Gray, 2009; Shutts, 2017; Weijenborg *et al.*, 2015, 2017), providing further theoretical ground to study interactions between convective-scale flow and the large-scale flow from the PV perspective.

However, a dominant role of upper tropospheric divergent outflow impinging on the jet has not (yet) been demonstrated explicitly. Such a dominant role is well established for other weather systems with strong latent heat release, tropical cyclones or warm conveyor belts, that interact with the jet (e.g., Grams *et al.*, 2011; Keller *et al.*, 2019; Riemer *et al.*, 2008). For convective systems, it is well known that convective variability, in particular in terms of convective organisation and amount of latent heat release, translates to variability in the divergent outflow aloft. In numerical models, when grid spacing is coarse and therefore convection needs to be parametrised, outflow variability tends to depend linearly on variability in latent heat release (Groot *et al.*, 2024). When convection is represented more realistically, and arguably in the real atmosphere, outflow variability depends nonlinearly on latent heat release (Bretherton & Smolarkiewicz, 1989; Groot *et al.*, 2024; Groot & Tost, 2023b; Mapes, 1993; Nicholls *et al.*, 1991). To our knowledge, only one study so far examines explicitly the role of divergent outflow for the downstream impact of a mesoscale convective system (Lojko *et al.*, 2022), but that study focuses on negative PV structures that are embedded in the outflow layer rather than displacement of PV gradients.

In the current study, we investigate the mechanisms that transition the initial uncertainties in convective systems into spread at large scales thoroughly. Thereby, it turned out to be impractical to follow the approach of Baumgart *et al.* (2019) and Selz *et al.* (2022) to use spatial composites of spread tendencies to describe the different contributions of each system to spread. Instead, we will focus on spread tendencies through a thoughtful examination of the spatial patterns of spread tendencies. The main questions that will be addressed are as follows: Does the multistage sequence of mechanisms (which holds in the mean) also apply to individual convective systems? And thus, by extension, is the advection of the PV gradient by the divergent flow indeed the most effective mechanism to project forecast spread onto the jet?

We address these questions by an ensemble spread-growth experiment covering a time period that encompasses the previously studied "Munich Hail Storm" event (e.g., Groot *et al.*, 2024; Wilhelm *et al.*, 2021). This period covers three simulated mesoscale convective systems that occur near the large PV gradient of the midlatitude jet over Europe in summer 2019. The ensemble is generated using initial condition uncertainty from the operational Integrated Forecast System (IFS). As in Selz *et al.* (2022), the IFS's initial perturbations are rescaled by a factor 1/1,000. Accordingly, moist-convective processes dominate early-stage spread growth (similar to Selz *et al.*, 2022). Essentially, our set-up ensures very fast initial divergence of the ensemble in regions of mesoscale convection and is thus suitable to analyse the upscale impacts arising from these convective regions.

Our analysis utilises, besides the PV diagnostic of Baumgart *et al.* (2019) and Selz *et al.* (2022), ensemble sensitivity analysis (ESA), combining the method with ideas from Groot *et al.* (2024). For coarse grid spacing (here, 13 km) and parametrised (deep) convection, mesoscale convection's outflow is nearly proportional to its precipitation rate and thus linearly correlated (Groot *et al.*, 2024), which translates to a linear correlation of the associated variability. In such a set-up, ESA can exploit the linear correlation to quantitatively link the ensemble's outflow variability with that of the precipitation rate (as a proxy of latent heat release). To make use of this quantitative link, the design of our spread-growth experiment judiciously includes a deterministic scheme to parametrise deep convection. Deterministic convection schemes underestimate spread growth (Plant & Craig, 2008; Selz *et al.*, 2022), and we thus expect that our ensemble experiment is underdispersive. Despite this caveat, and for the purpose of our current study, we consider the use of a deterministic scheme to be helpful for the interpretation of the mechanisms governing (upscale) spread growth.

In Section 2, we will summarise the methods of ESA and PV spread tendency diagnostics. In Section 3 we will introduce the meteorological setting of our experiments and the key convective systems. Furthermore, we will introduce the spread evolution at near-tropopause levels for this event. Section 4 presents our results, followed by a discussion and a final summary in Section 5.

2 | METHODS

2.1 | Simulation set-up

The selected episode is studied in the Icosahedral Nonhydrostatic (ICON) model at 26 km grid spacing over a global domain. A nest with 13 km grid spacing is used over Europe, with a two-way feedback between the nest and the global domain (Giorgetta *et al.*, 2018; Prill *et al.*, 2019; Zängl *et al.*, 2015). The configuration is largely the same as the deterministic run of the corresponding set-up in Groot *et al.* (2024) (see Table 1 for details), using mostly the standard parametrisation schemes. The simulations here, however, have been initialised based on initial conditions of the IFS ensemble on June 10, 2019, 1200 UTC. We run an ensemble of 50 perturbed members with one additional unperturbed member. All members are integrated out to 75 hr lead time (hr denotes hours lead time, from here on). Simulation output is stored every 30 min. The initial condition uncertainty is taken from the corresponding 50-member IFS ensemble, but has been reduced by a

TABLE 1 Key simulation settings.

Domain	Global domain	European nest
Model version	2.6.0	
Grid spacing (km)	26 (R03B06)	13 (R03B07)
Time step (s)	100	50
Altitude model top (km)	75	
No. vertical levels	90	
Deep convection scheme	Tiedtke (1989), Bechtold *et al.* (2014)	
Time step deep convection (s) and subgrid orography	1200	600
Time step gravity wave drag (s)	1200	
Microphysics scheme	1M (Seifert, 2008)	
Radiation scheme	Ritter–Geleyn	
Time step (s) radiation	1800	
Grid spacing (km), radiation	52	26
Rayleigh damping height (km)	22	
Initial conditions and ensemble perturbations	IFS ensemble analysis ×0.1% after Selz *et al.* (2022)	

factor 1,000 (constant in space), following Selz *et al.* (2022). The total ensemble spread is thus equal to 0.1% of the original (operational) forecast uncertainty. Thereby, our uncertainty regime closely resembles the intrinsic limit (Melhauser and Zhang (2012); Sun and Zhang (2016)), in which the whole upscale cascade and spread amplification (e.g. Selz *et al.* (2022); Durran and Gingrich (2014); Lorenz (1969)) is fully passed through over time (starting from the effective resolution). Thereby, it is assured that convective-scale variability considerably affects the uncertainty of the jet evolution, at least early on, and thus that the potential impact of the mesoscale convective variability for our selected cases can be meaningfully quantified.

The simulation output is stored at a 0.25° (about 28 km) output grid within the European nest; for the analysis of PV structures and their tendency diagnostics, regridding to a corresponding 0.75° resolution is applied (approximately the effective resolution) before all analyses are carried out, by means of bilinear interpolation using Climate Data Operator (Schulzweida, 2022). Apart from the associated noise removal, the leading-order tendency signals look broadly similar between the grids.

2.2 | Diagnostic tools

The two diagnostics used in this work are ESA (Ancell & Hakim, 2007; Torn & Hakim, 2008) and PV spread tendency diagnostics (Baumgart & Riemer, 2019). These diagnostics complement each other, and the combination of spatial structures in statistical signals and in PV tendencies strengthen our confidence in the diagnosed interactions between convective variability and the PV field. Our analysis focuses on near-tropopause dynamics. Hence, the PV spread tendencies are temporally averaged over 3 hr intervals and vertically over an isentropic layer with a thickness of 7.5 K, centred around $\theta = 331.25$ K. The ensemble sensitivity is carried out at 250 hPa.

The combination of tools allows us to identify the multistage uncertainty evolution over the course of a few days, starting near the intrinsic limit of initial uncertainty. Consequently, the role of processes in typical forecasting scenarios is not diagnosed. However, the role of convective variability in the downstream propagation of uncertainty can be assessed thoroughly.

2.2.1 | Ensemble sensitivity analysis

ESA is essentially a regression technique, which correlates patterns at $(x + dx, t + dt)$ with presumably correlated precursors at (x, t). Here, dt and dx consist of the spatio-temporal evolution of a (flow-dependent) pattern of variability, essentially a covariance pattern. Such a flow-dependent covariance pattern evolves with lead time (see also Magnusson, 2017). The associated lagged correlation is assessed by regressing across ensemble members. Insight into the variability of a pattern can be gained by inspecting the evolution of the pattern and by investigating its relation to plausible statistical precursors. The slope of the regression lines (relative to the

ensemble variance) expresses the estimated strength of the correlation between a pattern and another pattern (elsewhere). Their association can be quantified using covariance and correlation metrics. This slope is usually displayed in consecutive maps. By applying statistical testing to the correlations obtained, one may be able to distinguish correlation patterns of interest from random correlation patterns. A coherent set of ensemble sensitivity analyses may provide further insight into the chain of processes relevant for a certain pattern of variability (e.g., Groot & Tost, 2023a). Further examples of investigations of convective systems using ESA are, for instance, found in Hanley *et al.* (2013); Bednarczyk and Ancell (2015); Torn and Romine (2015); Magnusson (2017).

ESA will be applied to the magnitude of instantaneous mass divergence (i.e., outflow rate) in the upper troposphere, averaged over a box volume that covers the upper tropospheric part of a targeted convective system. Time windows of 3 hr are used for the diagnosis of mass divergence to filter out high-frequency variability in divergence signals and account for a time lag between mass divergence and downstream impact. Because the PV gradient is typically not (directly) co-located with the convective systems, it may take several hours for advected PV and gravity waves to reach the PV gradient.

2.2.2 | Quantitative PV perspective on spread growth

We consider Ertel (1942) PV, q, on isentropic levels:

$$q = \frac{\zeta + f}{\sigma}, \tag{1}$$

where ζ is the component of relative vorticity perpendicular to an isentropic surface, f is the Coriolis parameter, and $\sigma = -g^{-1}(\partial p/\partial\theta)$ is the isentropic layer density with gravity g, pressure p, and potential temperature θ. The local rate of change of PV is

$$\frac{\partial q}{\partial t} = -\mathbf{v}\cdot\boldsymbol{\nabla} q + \mathcal{N}, \tag{2}$$

where $\mathbf{v}$ is the horizontal wind, $\boldsymbol{\nabla}$ is the horizontal gradient on an isentropic level, and the non-conservative term $\mathcal{N}$ is

$$\mathcal{N} := -\dot{\theta}\,\frac{\partial q}{\partial\theta} + q\,\frac{\partial\dot{\theta}}{\partial\theta} + \frac{\nabla\times\dot{\mathbf{v}}}{\sigma}, \tag{3}$$

with diabatic heating rate $\dot{\theta}$ and non-conservative sources and sinks of momentum $\dot{\mathbf{v}}$. As in Selz *et al.* (2022), we decompose the horizontal wind in its purely rotational ($\mathbf{v_{rot}}$) and its purely divergent ($\mathbf{v_{div}}$) components:

$$\mathbf{v} = \mathbf{v}_{\mathrm{rot}} + \mathbf{v}_{\mathrm{div}}. \tag{4}$$

Our final partition of the PV equation can thereby be written as

$$\frac{\partial q}{\partial t} = -\mathbf{v}_{\mathrm{rot}}\cdot\boldsymbol{\nabla} q - \mathbf{v}_{\mathrm{div}}\cdot\boldsymbol{\nabla} q + \sum_i \mathcal{N}_i, \tag{5}$$

where $\mathcal{N}_i$ denotes the ith non-conservative process; for example, as represented by a parametrisation scheme in a numerical model. The basic idea (Davies & Didone, 2013) is to analyse the dynamics of the "difference" between two atmospheric states by the differences of the individual terms of the respective PV equation. As in Baumgart and Riemer (2019), we identify one state with the ensemble mean (denoted by an overbar) and the other state with an individual ensemble member. Indicating the deviation from the ensemble mean by Δ, considering (half of) the square of the PV deviation as a positive definite metric, and rearranging terms—see Baumgart *et al.* (2019); Selz *et al.* (2022) for details—we obtain

$$\frac{1}{2}\frac{\partial}{\partial t}(\Delta q)^2 = \mathrm{ADV}_{\mathrm{rot}} + \mathrm{ADV}_{\mathrm{div}} + \sum_i \Delta q\,\Delta\mathcal{N}_i + \mathcal{R}, \tag{6}$$

where $\mathrm{ADV}_{\mathrm{rot}}$ and $\mathrm{ADV}_{\mathrm{div}}$ denote the terms that are associated with advection by the non-divergent and irrotational wind respectively. These terms are given by

$$\mathrm{ADV}_{\mathrm{rot}} = \Delta q(-\Delta\mathbf{v}_{\mathrm{rot}}\cdot\nabla\overline{q}) \tag{7}$$

and

$$\mathrm{ADV}_{\mathrm{div}} = \Delta q\left(-\Delta\mathbf{v}_{\mathrm{div}}\cdot\nabla\overline{q} + \frac{1}{2}\Delta q\,\nabla\cdot\overline{\mathbf{v}_{\mathrm{div}}}\right). \tag{8}$$

Note that we have eliminated in this formulation the terms that merely redistribute $(\Delta q)^2$, instead of change its magnitude (see Baumgart *et al.*, 2018). In addition, we have introduced a residuum $\mathcal{R}$, which encapsulates discretisation and interpolation errors, and the non-conservative impact of numerical diffusion, which is not captured by model parametrisation (Baumgart *et al.*, 2018).

Based on Equation (6), it is straightforward to derive a tendency equation for ensemble variance (Baumgart & Riemer, 2019). More recently, this variance framework has also been used by Schmidt *et al.* (2025). Furthermore, note that the spread-growth formulation in Baumgart and Riemer (2019) and Selz *et al.* (2022), which is based on the sum over permutations of the differences between ensemble members, can be shown to be equivalent to a variance formulation.

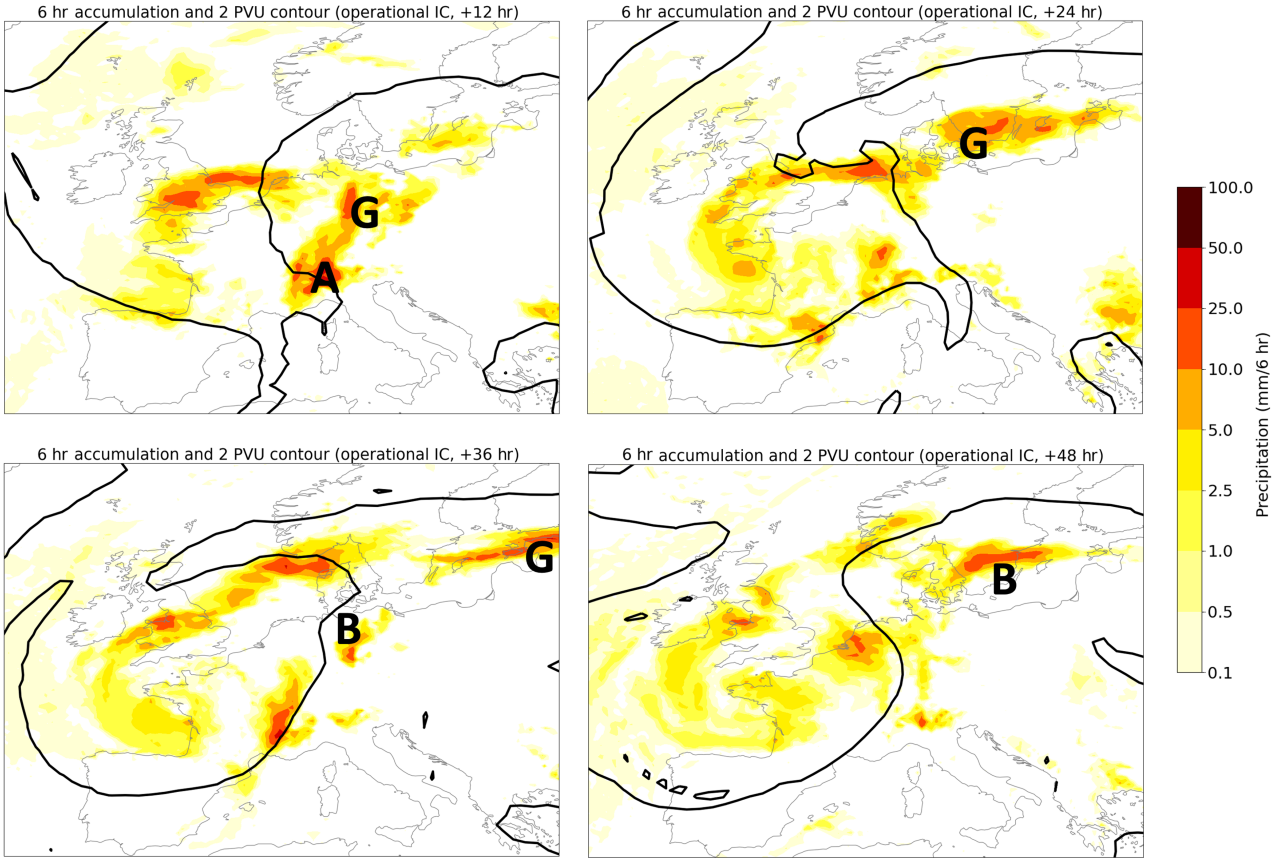

FIGURE 1 Accumulated precipitation over the past 6 hr for 12 hr (top left), 24 hr (top right), 36 hr (bottom left) and 48 hr (bottom right) forecasts of ICON (using the European Centre for Medium-Range Weather Forecasts Integrated Forecast System's operational run's initial conditions). The potential vorticity contour of 2 PVU at 250 hPa is contoured in black (coarse grained to 0.75°). Labels A, B, and G respectively mark the Alps convective system, the Baltic Sea convective system, and the Germany convective system. [Colour figure can be viewed at wileyonlinelibrary.com]

In summary, we arrive at a tendency equation that quantifies the individual contributions to the evolution of ensemble variance associated with PV advection by the non-divergent wind (hereafter referred to as rotational tendency), associated with PV advection by the irrotational wind (hereafter referred to as divergent tendency), and the nonconservative tendencies due to parametrisation schemes. We will explicitly present tendencies from the deep convection and the long-wave radiation scheme. Tendencies from the grid-scale precipitation and short-wave radiation schemes have been found to be of subordinate importance and will not be shown. Previous work (Baumgart *et al.*, 2019) found that tendencies from other parametrisation schemes (turbulence, gravity wave drag) are negligible compared with convection and have thus not been considered in this study.

The tendency diagnostics are computed over the 13 km European nest only. The spherical harmonics package Windspharm (Dawson *et al.*, 2018) for Python has been utilised to split the wind into rotational and divergent wind components, following Equation (4).

3 | SYNOPTIC OVERVIEW AND INITIAL PV SPREAD

3.1 | Synoptic setting

Investigating the interaction of divergent convective outflow with the strong PV gradient associated with the midlatitude jet requires that mesoscale convective systems occur in proximity to that gradient. From June 10 to 12, 2019, a previously studied period (Groot *et al.*, 2024; Wilhelm *et al.*, 2021), convection presumably fulfils this requirement. During this period, southerly flow ahead of an upper level trough over France advected warm and moist air over the European continent (not shown), favouring the formation of deep convection. Three organised convective systems occurred ahead of the trough and within the downstream ridge, while the upstream trough underwent cyclonic wave breaking (Figure 1).

On June 10, one convective system occurred very close to the upper level trough over the western Alps (hereafter referred to as the Alps system; labelled "A" in Figure 1a).

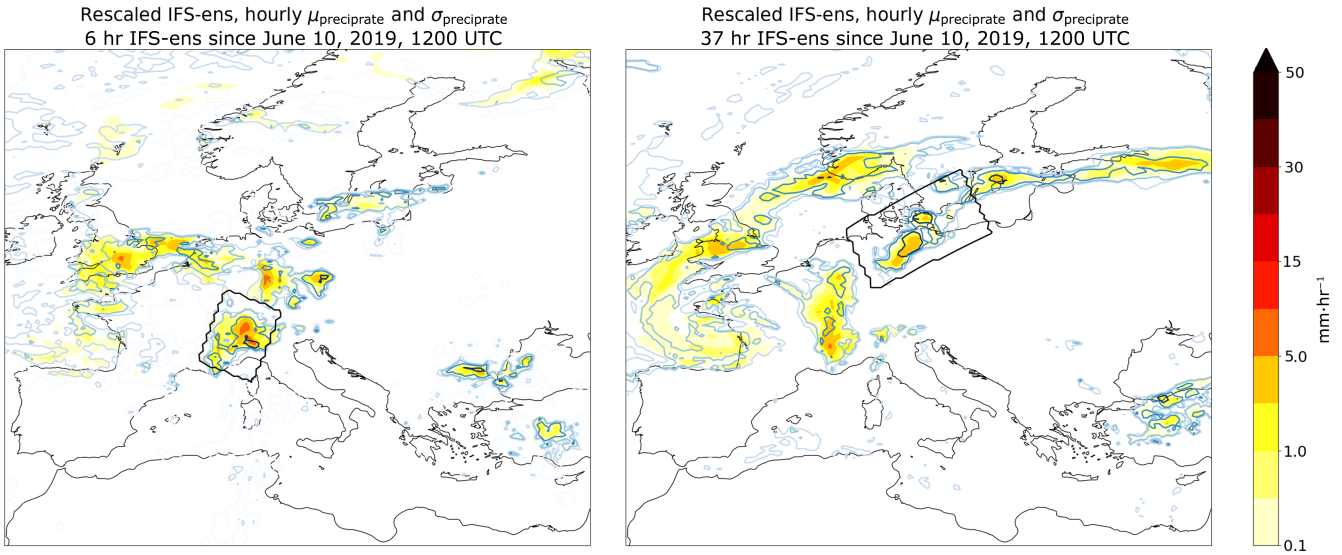

FIGURE 2 Mean precipitation rates (fill) and spread in mean precipitation rate (isolines) at approximately the time of maximum intensity for (left) the Alps system and (right) the Baltic Sea system. Spread is contoured at grid values of 0 (i.e., precipitation occurs in some ensemble members), 0.01, 0.05, 0.25, and 1 mm · hr^{-1}. The masks (black outline) defining the extent of each convective system are also visualised at this (approximate) time of maximum intensity. [Colour figure can be viewed at wileyonlinelibrary.com]

At the same time, a second system initiated farther downstream of the trough over Germany. This system subsequently moved northward into the Baltic Sea and then further downstream (hereafter referred to as the Germany system; labelled "G" in Figure 1a–c). A third mesoscale convective system initiated during the night of June 11–12 over northern Germany, and subsequently moved northward over the Baltic Sea region (hereafter referred to as the Baltic Sea system; labelled "B" in Figure 1c,d). All three convective systems have their main outflow at upper tropospheric levels—about 200–300 hPa (see also Groot, 2023; Groot *et al.*, 2024)—and will be shown to interact with the PV gradient associated with the jet stream, and their variability plays a prominent role in the evolution of ensemble spread. The nature of their interaction and the mechanisms that govern spread growth will be the focus of Sections 4.1–4.3. We limit our analysis to the first 3 days of our experiment, because the main direct impact of the divergent outflow on the spread evolution occurs during the first 2–3 days in comparable experimental configurations (Baumgart *et al.*, 2019; Selz *et al.*, 2022).

3.2 | Characteristics of the convective systems

As introduced in Section 2, we describe characteristics of the convective systems by defining a region for the respective system, over which quantities are averaged. The horizontal extents of these regions are displayed in Figure 2. For the Alps system, the region remains fixed. For the Baltic Sea system, the averaging region moves with the convective system with a constant northeastward translation speed. A representative relative position of the region's boundary with respect to the embedded precipitating area is shown in Figure 2b. The boxes do not have equal volumes; they just span a rectangular area around a convective system. For the Germany system, our analysis of PV tendency diagnostics in Section 4 does not indicate that convective variability directly projects onto variability of the strong PV gradient by variability of the convective outflow. Because convective variability of this system is not associated with variation in the evolution of the PV gradient downstream, we refrain from an ESA using convection characteristics and, consequently, herewith we omit the definition of an averaging region for that system.

Based on our averaging regions, the Alps system in our ICON experiments exhibits a mean precipitation rate of about 1.0 mm · hr^{-1} during its initial stage, first decaying to less than 0.7 mm · hr^{-1} after about 13 hr into the experiment, followed by further decay. The Alps system accumulates 15 mm of precipitation, of which 9.4 mm falls between 2 and 13 hr lead time. The key event on day 2 is the development of the Baltic Sea system (Figure 2). Shortly after its initiation over central Germany (after about 31 hr), its precipitation rate doubles between 34 and 36 hr over northern Germany. While moving to the Baltic Sea, the mean precipitation rate fluctuates between 0.22 and 0.42 mm · hr^{-1}. Despite the lower intensity, appreciable precipitation (3.6 mm accumulation on average) occurs over a notably larger area than covered by the Alps system.

TABLE 2 Accumulation and spread in rainfall in two convective systems.

Name	Alps system	Baltic Sea system
T_{start} (hr)	2	31
T_{end} (hr)	13	46
Duration (hr)	11	15
Accumulated rainfall (mm)	9.4	3.6
Ensemble spread accumulated rainfall (mm)	0.04	0.10
Dimensionless ensemble spread rainfall	0.004	0.03

Consistent with very small initial condition uncertainty, and the use of a deterministic convection scheme, the spread in the precipitation associated with the two systems is very small: 0.4% and 3% relative to their respective mean precipitation (Table 2). Despite this small relative spread, both systems can be identified as distinct features in the PV spread at the time of their occurrence, and PV-spread tendencies can be clearly associated with these systems (see later). Furthermore, we note that the relative spread of the Baltic Sea system, which occurs on day 2 in our experiments, is an order of magnitude larger than that of the Alps system, which occurs on day 1. This order-of-magnitude difference is consistent with exponential initial spread growth; that is, while spread is still small and far from saturation, and very short spread-doubling times in convective regions (order of hours; e.g., Hohenegger & Schar, 2007; Selz & Craig, 2015; Weyn & Durran, 2017; Groot & Tost, 2023a). It is illustrative for the tiny magnitude of our (convective) forecast spread, despite the lead time of $\sim$ 36 hr.

The spread of convective outflow is very similar to that of precipitation, as in Groot *et al.* (2024) (here further demonstrated by results shown in Appendix A). Our analysis in Section 4 therefore focuses on the relation between outflow and PV variability, without further explicit consideration of precipitation variability.

3.3 | Overview of spread evolution

We provide an overview of the spread evolution in our spread-growth ensemble experiment on isentropic levels intersecting the dynamical tropopause in Figure 3. This figure will further serve as reference when discussing our process-based analysis of the spread evolution in Section 4.

Early during the experiment (until 9 hr; Figure 3a–c), spread is predominantly associated with the Alps and Germany systems. Subsequently, spread over the Germany system amplifies strongly but remains localised in the vicinity of the system. Spread associated with the Alps system seemingly extends downstream (northward) along the strong PV gradient associated with the upstream trough and eventually amplifies during the cyclonic wrap up of the trough (Figure 3d–f). At 24 hr, spread associated with the trough and with the Germany system constitute prominent spread maxima (Figure 3d–f). On day 2 of our experiment (Figure 3g–j), the spread associated with the Germany system is being advected downstream without prominent further amplification, whereas the spread associated with the trough wraps up cyclonically within the trough and exhibits limited impact on the downstream ridge.

Associated with the Baltic Sea system, a new local spread maximum emerges around 36 hr over northern Germany (Figure 3h), subsequently moving over the Baltic Sea (42–48 hr; Figure 3i,j). This spread maximum apparently couples with the strong PV gradient and amplifies while propagating downstream (54–60 hr; Figure 3k,l). Late in our experiment (exemplified at 60 hr in Figure 3l), spread is predominantly located in the vicinity of the strong midlatitude PV gradient. For completeness, we note that spread has developed also in the southeast of our domain, originating from convection in that region (as indicated in Figure 3). This spread is of lower amplitude than that over western and northern Europe (at least on the isentropic levels examined) and does not interact with the strong midlatitude PV gradient in any obvious way. Therefore, spread evolution in that region of our domain is not relevant to this study.

4 | RESULTS: ANALYSIS OF SPREAD DYNAMICS

In Sections 4.1–4.3 we analyse the PV-spread tendencies associated with the three convective systems introduced in Section 3.2. In addition, we employ ensemble sensitivity to link convective variability with ensuing PV variability along its near-tropopause gradients. Both analyses have been carried out over the full European nest (13 km grid spacing) and are furthermore regridded to 0.75° grid spacing for the analysis (approximately the effective resolution). Our focus with these analyses will be on the three-stage sequence of spread-growth processes as identified by Baumgart *et al.* (2019); Selz *et al.* (2022) and described in Section 1. In addition to the three dominant processes emphasised in these previous studies—that is, the tendencies from the deep-convective scheme (stage 1) and their transition to divergent mode (mostly stage 2) and later rotational mode (mostly stage 3)—we will find a substantial contribution of long-wave

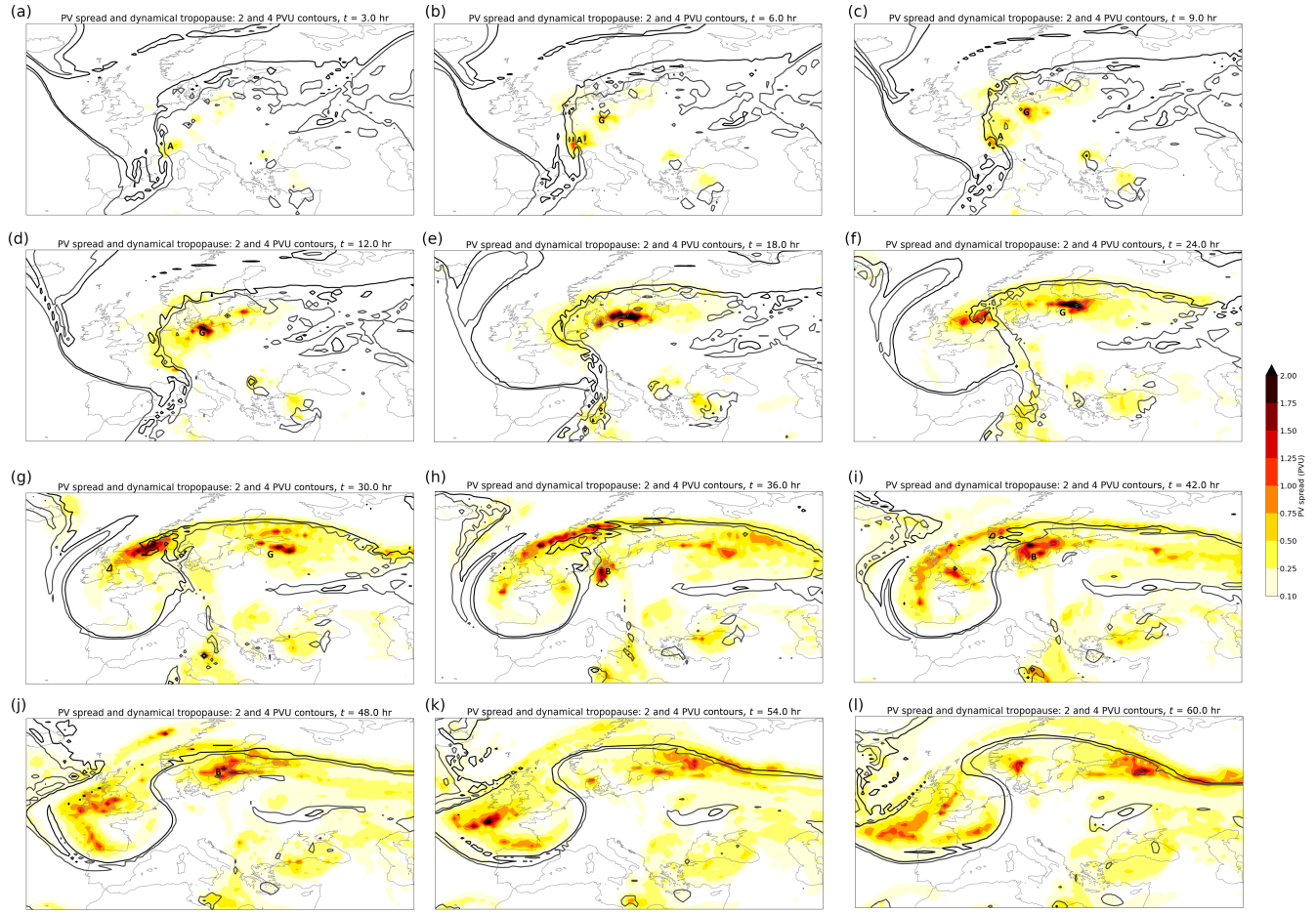

FIGURE 3 Evolution of 2 and 4 PVU contours at 330 K (ensemble mean) with potential vorticity spread at 327.5–335 K superposed (colour fill) at 3 hr intervals (initially) and 6 hr intervals (beyond 12 hr). Labels A, B, and G respectively mark the Alps convective system, the Baltic Sea convective system, and the Germany convective system. [Colour figure can be viewed at wileyonlinelibrary.com]

radiative tendencies occurring in close relation to convective activity. In Section 4.4 we thus examine this relation in some more detail. It turns out that tendencies due to grid-scale precipitation and short-wave radiation are typically small and tend to reduce spread (if active at all). Throughout Sections 4.1–4.3, we present 3 hr averages of selected intervals, which are typically representative of nearby intervals and a smooth evolution (unless it is indicated they are not).

4.1 | Alps convective system

The first spatially coherent signal of spread-growth rates in the vicinity of the Alps system occurs after 3–6 hr (Figure 4; note that we illustrate 3 hr average growth rates for optimal clarity). Growth rates due to the deep-convective scheme dominate in the vicinity of the Alps system at this early stage of spread growth (Figure 4a), in close proximity to the jet stream (2 and 4 PVU contours) and matching with the area of PV spread (cf. Figure 3). Divergent spread growth also occurs in the vicinity of the Alps system, but with much smaller amplitude (Figure 4c). Nonlinear spread growth is negligible (Figure 4d). The early-stage spread growth near the Alps system is thus confirming dominance of a first spread-growth stage, in line with Baumgart *et al.* (2019); Selz *et al.* (2022), and of Zhang *et al.* (2007).

We further note that long-wave radiative tendencies make a notable contribution to spread growth near the Alps system (Figure 4b). The magnitude of the associated growth rates is larger than that of the divergent tendencies and somewhat smaller than that of the deep-convective scheme, and all three overlap spatially. On the broader scale, the long-wave radiative tendencies exhibit a remarkable spatial consistency with the convective tendencies (cf. Figure 4a,b) and, overall, are of similar magnitude. This general spatial consistency persists over the next 15 hr and can be observed also at 15–18 hr (Figure 6a,b). The vertical structure of their close relationship will be discussed in more detail in Section 4.4 for one convective system.

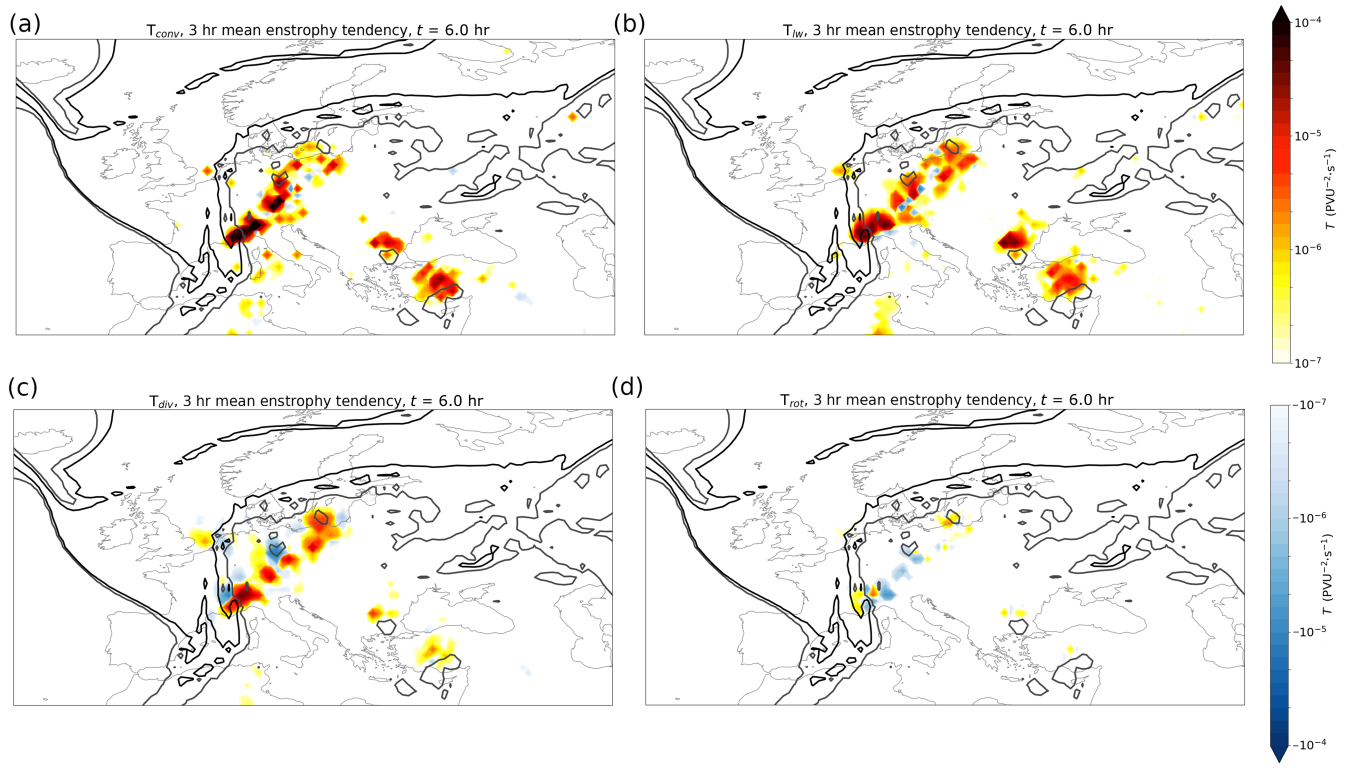

FIGURE 4 The 3 hr mean of the potential enstrophy tendency for two different processes at θ of 327.5–335 K, $t = 6$ hr: (a) heating by the deep convection parametrisation, (b) heating by long-wave radiation parametrisation, (c, d) the differential potential vorticity (PV) advection resulting from differences in (c) divergent winds and similarly for (d) the rotational winds. Colours displayed in the colour bar of the upper and bottom rows. For this level, the dynamical tropopause (2 PVU) and 4 PVU contour are also shown in dark grey/black. [Colour figure can be viewed at wileyonlinelibrary.com]

It is difficult to discern a period when spread growth associated with the Alps system is dominated by divergent tendencies; that is, it is difficult to identify the dominance of the second stage of the three-stage models of (Baumgart *et al.*, 2019; Selz *et al.*, 2022; Zhang *et al.*, 2007). After dominant early-stage spread growth by deep convective tendencies, the divergent tendencies exhibit a rather complex pattern of alternating positive and negative values (exemplified at 15–18 hr in Figure 6c), in particular in the region of the spread associated with the Alps system located on the northeastern flank of the upstream trough (cf. Figure 3a–e). Visual inspection of divergent spread tendencies at intermediate times strongly indicates that the alternating pattern is associated with inertia–gravity waves emanating from the Alps system and the German system (not shown), which fills the region of this ridge over central Europe. The wave-like pattern of the divergent tendencies prohibits a straightforward interpretation of its impact on the spread associated with the Alps system and the PV gradient in its proximity. Regardless, it is not obvious from visual inspection whether the positive values of divergent tendencies on the northeastern flank or rotational and long-wave radiative tendencies net dominate this region.

It is noteworthy that long-wave tendencies in the spread region associated with the Alps system do not coincide spatially with deep convective tendencies at 15–18 hr (cf. Figure 6a,b). Visual inspection of intermediate times (not shown) reveals that this local maximum of long-wave tendencies can be traced back to the Alps system. Apparently, long-wave radiative tendencies outlive convective tendencies there, after the convective system has ceased. In the rest of the domain, long-wave radiative tendencies spatially coincide with convective tendencies as at 6 hr, but long-wave tendencies are now mostly of larger magnitude than the deep convective tendencies.

To further explore the relation between the variability of convective outflow with PV spread we employ ESA. This analysis shows that the strength of the divergence over the Alps system and PV values along the adjacent large PV gradient over eastern France are associated with each other (Figure 5a). The analysis thus directly quantifies the link between the variability in convective activity of the Alps system and nearby jet variability. However, since dipole patterns are seen and absolute linear correlations are not uniform, there is no suggestion of a direct linear link between the two, indicating no uniform connection

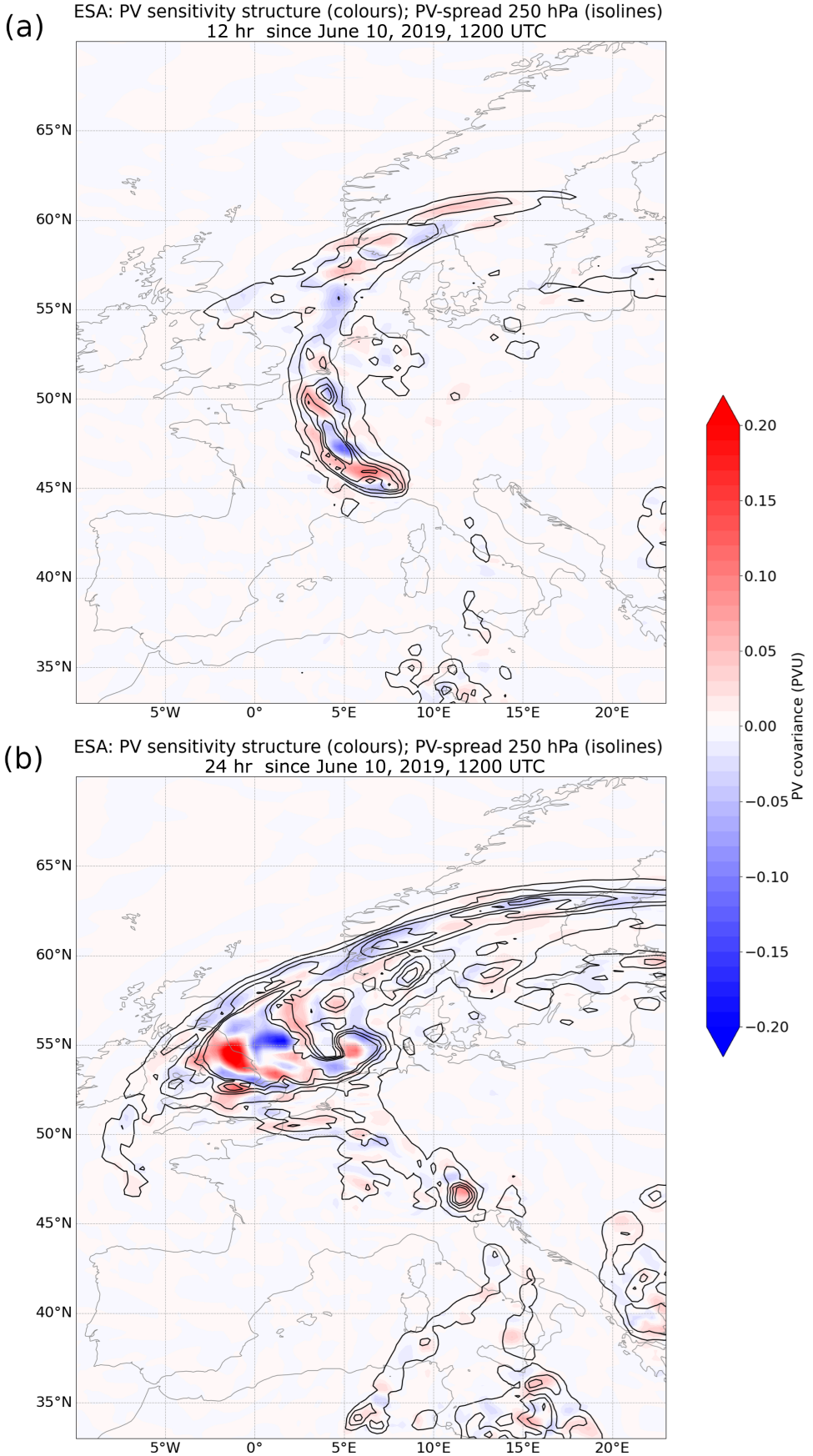

FIGURE 5 Potential vorticity (PV) covariance at 250 hPa within the ensemble associated with enhanced mass divergence in the upper troposphere over the convective system in the Alps between 2 and 5 hr simulation time: (a) 12 hr; (b) 24 hr. Isolines indicate regions of enhanced σ_{PV} within the ensemble (isolines at 0.06 PVU intervals between 0.06 and 0.30 PVU). ESA: ensemble sensitivity analysis. [Colour figure can be viewed at wileyonlinelibrary.com]

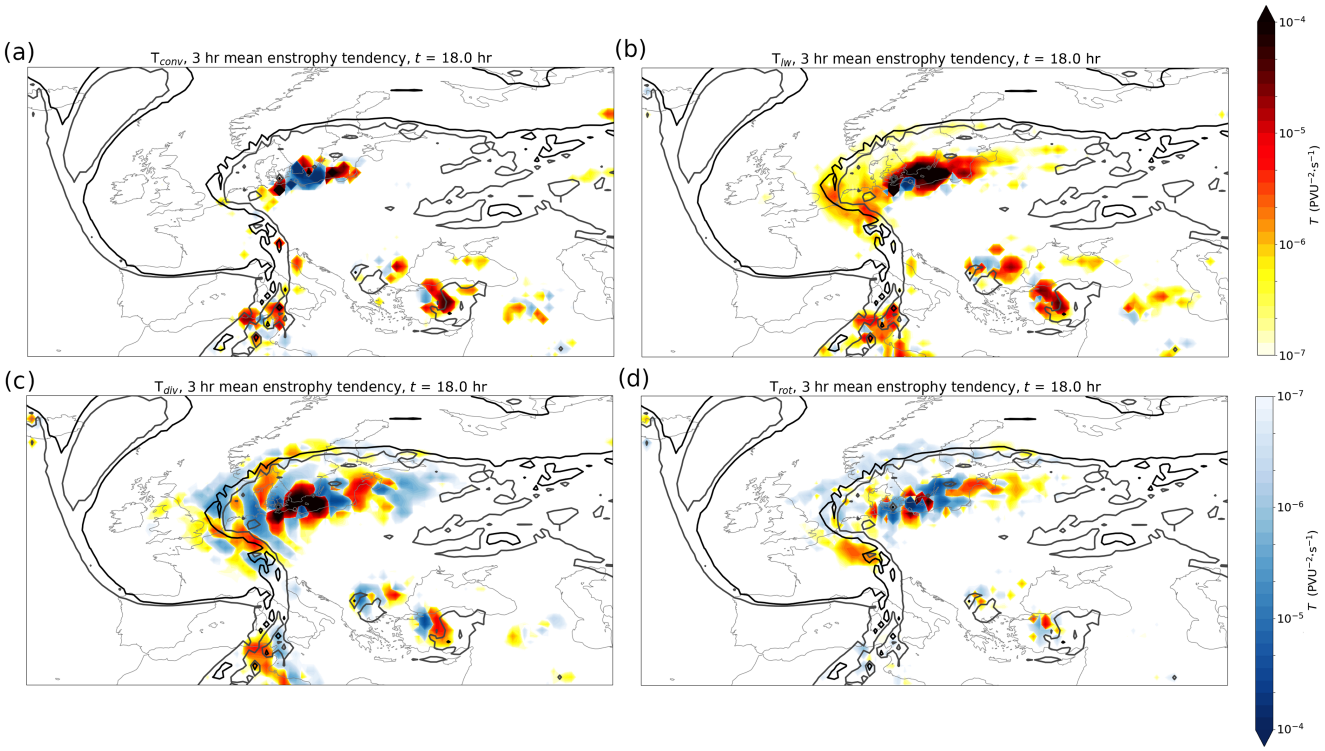

FIGURE 6 As in Figure 4: 3 hr mean of the potential enstrophy tendency for four different processes at θ of 327.5–335 K, t = 18 hr. [Colour figure can be viewed at wileyonlinelibrary.com]

between outflow rates of the Alps system and adjacent reduced PV values. Such a uniform area of negative correlations would be expected if stronger outflow were associated with a stronger displacement of PV contours from the ridge towards the trough, thereby leading to reduction of PV in the region of displacement.

Our interpretation of the alternating positive and negative correlations of the sensitivity analysis is that they indicate a downstream propagation of a more localised perturbation of the jet by the Alps system (as indicated in Figure 5a–c). Despite this double dipole pattern, the convective outflow rate has a significant correlation with a reduction of the mean PV over the spread maximum in eastern France—at least after 12 hr at the expected time lag, although barely reaching the significance threshold. The ESA thus confirms that variability in the convective activity of the Alps system generally translates to spread along the adjacent jet. The rich regional substructure, however, seemingly related to a more localised impact of the Alps system, does not support the notion that divergent tendencies dominate spread growth associated with the Alps system for a certain period of time; that is, there is no clear evidence for the occurrence of a distinct second stage of three-stage spread growth for the Alps system.

The third stage of spread growth, according to Baumgart *et al.* (2019); Selz *et al.* (2022), is dominated by rotational tendencies. At 15–18 hr, the rotational tendencies have clearly amplified in absolute values since at 3–6 hr. The northeastern flank of the trough is a region of spatially coherent positive tendencies, clearly linked to the local spread maximum initiated earlier by the then occurring Alps system (Figure 6d), although the convection itself has now mostly deactivated. This coherent spread growth indicates the highly nonlinear evolution of the trough (i.e., wave breaking), because nonlinearity in the underlying dynamics is required for spread amplification by rotational tendencies (Baumgart *et al.*, 2018). Despite spatial coherency, the rotational tendencies are very localised and, hence, cannot dominate spread growth on the flank of the trough at 15–18 hr. Subsequently, the trough completes its cyclonic breaking and spread amplifies within and spreads across the broken trough (Figure 3e–j). The tendencies depicted at 33–36 hr in Figure 7 are representative of the relative importance of individual contributions to spread growth associated with the trough. Overall, the tendencies exhibit complex patterns, but it is clear that the rotational tendencies do not dominate spread growth in the trough region. Owing to the dominant contributions by long-wave tendencies at this time, which cannot be traced back to the Alps system, it is clear that the further generation in the trough has little origin (if any at all) in the convective uncertainty associated with the Alps system.

In summary, the evolution of spread associated with Alps systems only partly exhibits signatures of

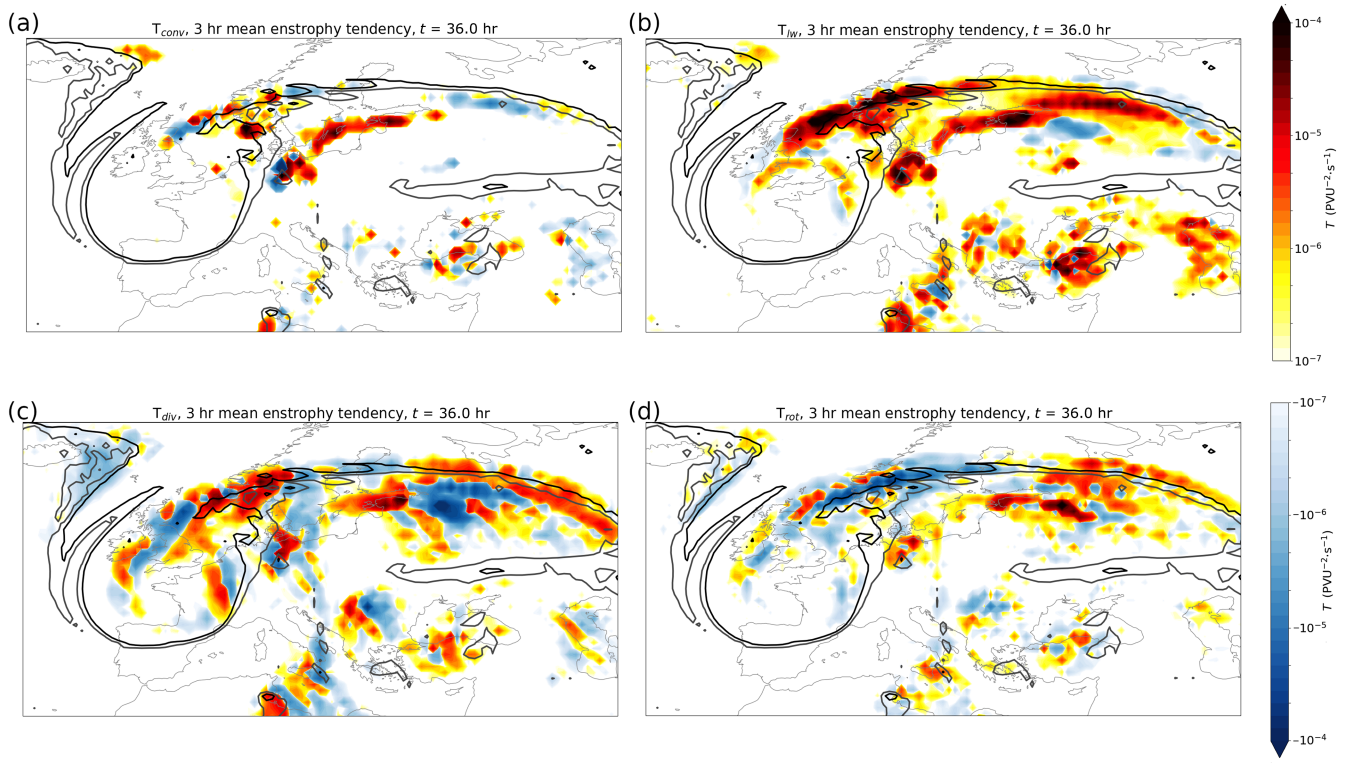

FIGURE 7 Same quantities as in Figure 4; 3 hr mean of the potential enstrophy tendency for four different processes at θ of 327.5–335 K, t = 36 hr. [Colour figure can be viewed at wileyonlinelibrary.com]

the hypothesised sequence of events identified from diagnostics after averaging by Baumgart *et al.* (2019); Selz *et al.* (2022). Convective tendencies dominate initial spread growth (an indication of stage 1). Indicating a presumed transition to stage 2, divergent tendencies generate PV spread along the strong PV gradient adjacent to the Alps system. Rotational tendencies further amplify the existing spread by nonlinear dynamics along the PV gradient, indicating the onset of stage 3. Despite these consistencies with the conceptual sequence, subsequently, divergent and rotational tendencies do, nevertheless, not play a sustained, dominant role. Hence, pronounced and distinctive fingerprints of stages 2 and 3 cannot be identified. Arguably, nonlinear spread growth did not have the time to become a dominant mechanism, because of the cyclonic breaking of the upstream trough. This breaking effectively limited downstream dispersion and associated further amplification of spread by rotational tendencies. In addition, long-wave radiative tendencies made a substantial contribution to the spread evolution throughout the period considered, further complicating the identification of a three-stage sequence. Finally, significant interaction between the Alps system and the PV gradient is suggested by both of our analyses methods.

4.2 | The Germany system and its spread evolution

Spread associated with the Germany convective system develops early in the experiment over Germany (at 3–6 hr and 6–9 hr; Figure 3a–c, cf. Figure 2a). Subsequently, moving northeastward within the ridge over central Europe (closer to the PV gradient), this spread region constitutes the distinct maximum of the spread distribution until 24–27 hr (Figure 3c–f). Moving along the zonally oriented, strong PV gradient over northeast Europe (30–42 hr; Figure 3g,i), the maximum tends to weaken and there is no clear net amplification of spread when interacting with the jet. At the end of day 2, spread associated with the Germany system has essentially moved out of the domain under consideration.

Similar to the Alps system, initial spread growth over the Germany system is dominated by deep convective tendencies, accompanied by a secondary contribution of long-wave radiative tendencies (Figure 4a,b). The first, convective stage of spread growth is thus again evident. In contrast to the Alps system, divergent tendencies subsequently make a clear and strongly positive contribution to spread growth above the Germany system: though positive and negative values, supposedly associated with the

inertia–gravity waves, fill most of the ridge over Europe, divergent tendencies remain strongly positive just above the Germany system for the remainder of day 1 (illustrated in Figure 6c at 15–18 hr). Meanwhile, net amplification of spread by deep convective tendencies has clearly decreased over the system (Figure 6a). The inertia–gravity wave pattern extends to the strong PV gradient associated with the jet (between the North Sea and the Baltic Sea; Figure 6c). At a fixed location, however, the sign of the tendency alternates with time (not shown). The characteristics of divergent tendencies remain qualitatively similar during day 2 (not shown), whereas the Germany system is moving somewhat closer to the strong PV gradient (exemplified at 33–36 hr in Figure 7c): the divergent tendency pattern is complex, with large positive values above the active convection of the system but no persistent positive values along the strong PV gradient closest to the system, and hence with no remote impact on that gradient.

In contrast to the divergent tendencies, rotational tendencies are positive along the PV gradient near the eastern part of the spread maximum associated with the Germany system on day 2 (Figure 7d, cf. 3h). This signal suggests that an interaction between the convective system and the jet occurs by the variability of the rotational wind that is in balance with the PV spread generated by the convective system. As noted earlier, however, this interaction does not excite further substantial net amplification of spread along the jet within our integration domain. Before the associated spread pattern leaves the domain, the dominant spread source manifesting spread growth does not originate from rotational tendencies, which would represent stage 3 of the conceptual spread growth model (Baumgart *et al.*, 2019; Zhang *et al.*, 2007).

Similar to the Alps system, the long-wave tendencies of the Germany system make an important contribution to spread growth, both on day 1 and day 2 (Figures 4 and 6b, and Figure 7b respectively). At 15–18 hr, in particular, long-wave tendencies are at least as strong as divergent tendencies (cf. Figure 6b,c). Illustrated at 33–36 hr, we note again that long-wave tendencies overlap strongly with convective tendencies (cf. Figure 7a,b).

In summary, we interpret the salient features of the spread evolution associated with the German convective system as follows. A first stage of spread growth is dominated by deep convective tendencies and a second stage by divergent tendencies. The second stage, however, is not characterised by an interaction of convective outflow with a strong PV gradient. A plausible explanation for this lack of interaction is that the convective system is still too far away from the jet. We suggest that the local spread growth by divergent tendencies above the convective system relates to the adjustment of convective outflow to a balanced anticyclone (Bierdel *et al.*, 2017, 2018), which is thus more akin to a second stage of spread growth as suggested by Zhang *et al.* (2007) than to the sequence of Baumgart *et al.* (2019). Along the same line, we interpret subsequent rotational tendencies along the strong PV gradient as an interaction of this anticyclone with the jet, which indicates the potential beginning of the third stage of spread growth dominated by rotational tendencies—according to Baumgart *et al.* (2019); Selz *et al.* (2022). This stage, however, is not realised here, at least not within the domain of our experiment. We attribute the observed lack of subsequent spread growth by rotational tendencies to the rather straight orientation of the jet, which implies linear dynamics of perturbations on the jet. Nonlinear (Rossby wave) dynamics, however, are required for further spread amplification by rotational tendencies (Baumgart *et al.*, 2018), and such a contrasting scenario will be exemplified later herein by the spread evolution downstream of the Baltic Sea system on day 3.

4.3 | The Baltic Sea system

Spread associated with the Baltic Sea system first occurs as a distinct maximum in the spread distribution around 36 hr over northern Germany (Figure 3g; cf. Figure 2c). This spread maximum grows rapidly in the next 6–12 hr and becomes dominant in the ridge over Europe, whereas the convective system is moving over the Baltic Sea and towards the strong PV gradient associated with the jet (Figure 3h,i, cf. Figure 2d). Note that, just before interaction with the strong PV gradient, spread is very limited along the PV gradient in the vicinity of the Baltic Sea system, as well as in the adjacent downstream region (Figure 3i), because previous spread sources have left few traces (if any) of downstream impact here. After interaction, spread amplifies along the strong PV gradient (Figure 3k,l). It is therefore feasible to examine the conceptual three-stage sequence of spread growth in the context of the spread evolution associated with Baltic Sea system, despite the relatively late initiation of that system on day 2 in our experiment.

Just after the initiation of the Baltic Sea system, a first, convective stage of spread amplification occurs, evidenced by deep convective tendencies dominating over divergent and rotational tendencies in the vicinity of the system (shown at 33–36 hr in Figure 7a,c,d; cf. Figure 2c). Similar to the Alps and the Germany system, long-wave tendencies make a further prominent or even dominant contribution to spread amplification near the Baltic Sea system at this early stage (Figure 7b). Spatial patterns are consistent with the patterns we identified for the earlier systems (Sections 4.1 and 4.2). Subsequently, during the second half of day 2, deep convective tendencies persist and

divergent and rotational tendencies increase near the system (not shown), suggesting the onset of stage 2 of spread growth. More importantly, the Baltic Sea system exhibits a clear signature of interaction with the strong PV gradient by its convective outflow, first (at 42 hr) with positive divergent tendencies occurring predominantly along the gradient near the system. They persist until well beyond 45 hr (not shown). The Baltic Sea system thereby exhibits a clear signature of the second stage of spread growth according to our interpretation of the three-stage sequence of Baumgart *et al.* (2019). In the following, we use the ESA to demonstrate and quantify the relation between variability in the convective outflow and PV variability along the strong PV gradient.

Figure 8b,d,f shows the PV deviation associated with enhanced divergent outflow over the convective system that moves from northern Germany into southern Scandinavia. After 34 hr, a negative covariance between PV and the divergent outflow strength at 250 hPa arises in a region with about 0.4 PVU spread (Figure 8b); it is co-located with the Baltic Sea system developing over Germany and indicates statistical association of enhanced convective outflow with negative local PV deviations within the ensemble, which from a PV perspective apparently occurs because of the following sequence. When convection and precipitation are amplified in a certain ensemble member, this amplification relates to amplified convective heating in the middle troposphere in a certain simulation (see also Section 3.2). Accordingly, enhanced mid-level heating is within the ensemble correlated with enhanced upward advection of an air mass with low PV, followed by transport towards its surroundings; for instance, towards the jet stream (i.e., causing strengthening of divergent winds towards a PV gradient). Correspondingly, our growing and amplifying feature with a negative PV deviation indeed moves northward into southwestern Sweden towards a strong PV gradient (39 hr; Figure 8d) and lies along 60° N by 44 hr (Figure 8f). The correlations in Figure 8 are generally low everywhere at 34 hr ($|r| < 0.5$), except locally in proximity of the mesoscale convective system (Figure 8a,b,e); these areas can be assumed to be affected by outflow of the mesoscale convective system. At 44 hr, ESA correlations $|r|$ are low except for southern Scandinavia.

As an aside, we note that, despite the dominant negative deviation PV behaving as expected, positive deviations are also visible in Figure 8 after 39 and 44 hr. Non-monotonic bands of PV correlations with the divergent outflow intensity are indeed expected along the gradient where the PV gradient is not single-signed, travelling in a fixed direction. The local existence of the double PV gradients over central- Sweden and central Norway after about 42 hr, for instance, is recognised from the folded PV isolines in Figure 3h,i. The transient interaction with the jet stream's double PV gradient is responsible for PV dipoles along the jet stream here (not shown).

The PV variability on day 3 as associated with strengthened mass divergence from the Baltic Sea system at 34–37 hr is displayed in Figure 9. Here, we demonstrate the evolution after the northward jet shift over central Sweden (which occurs at 44 hr). Whereas the PV perturbation follows the jet stream downstream for the next 24 hr into Finland and Russia, a wave pattern develops with smaller positive PV perturbations at both flanks of the negative branch. The positive correlations forming downstream of the negative correlations indicate downstream dispersion akin to a Rossby wave packet. Similar Rossby-wave-like dispersion of spread has been documented by several previous studies (e.g., Anwender *et al.*, 2008; Parsons *et al.*, 2019; Riemer *et al.*, 2008). Quantitatively, the negative PV deviation associated with the wave pattern has considerable amplitude throughout its residence (within our European nest), with co-variability in PV of up to about 0.8–1 PVU (Figure 9). Furthermore, the local correlation coefficient between upper tropospheric divergence on the previous day and PV at the jet stream's gradient exceeds 0.7 in the core region, linking about half of the PV variability with the differences in convective (out)flow rate of the Baltic Sea system. The corresponding association between precipitation rate and the Rossby-wave-like perturbations is investigated in Appendix A. In contrast to the Alps system, here, the association is easily tracked downstream with linear analysis. Our correlation pattern maximises within the spread maximum and reaches the eastern boundary of our nest by 72 hr (Figure 9f). In summary, strong correlations overlapping with a shifted jet signify high robustness. Correspondingly, outflow variability projects strongly on the downstream development of the jet stream over Finland and Russia. As hypothesised, from a mechanistic perspective, intenser (divergent) advection following high-amplitude convective heating displaces the jet stream outward (here, northward), followed by Rossby dispersion.

While propagating downstream, spread further amplifies along the strong PV gradient by nonlinear dynamics. Indicating the onset of a third stage of spread growth, rotational tendencies along the strong PV gradient in the vicinity of the Baltic Sea system first become evident around 45 hr in the region. Here, rotational tendencies overlap with pre-existing divergent tendencies (not shown) as the convective outflow starts to interact with the PV gradient (Figure 10a; cf. Figure 8e,f), which amplifies rotational tendencies strongly in the next 3 hr and beyond (Figure 10b–f). The increasing importance of rotational tendencies is in contrast to the evolution of spread downstream of the Germany system. We attribute this distinct

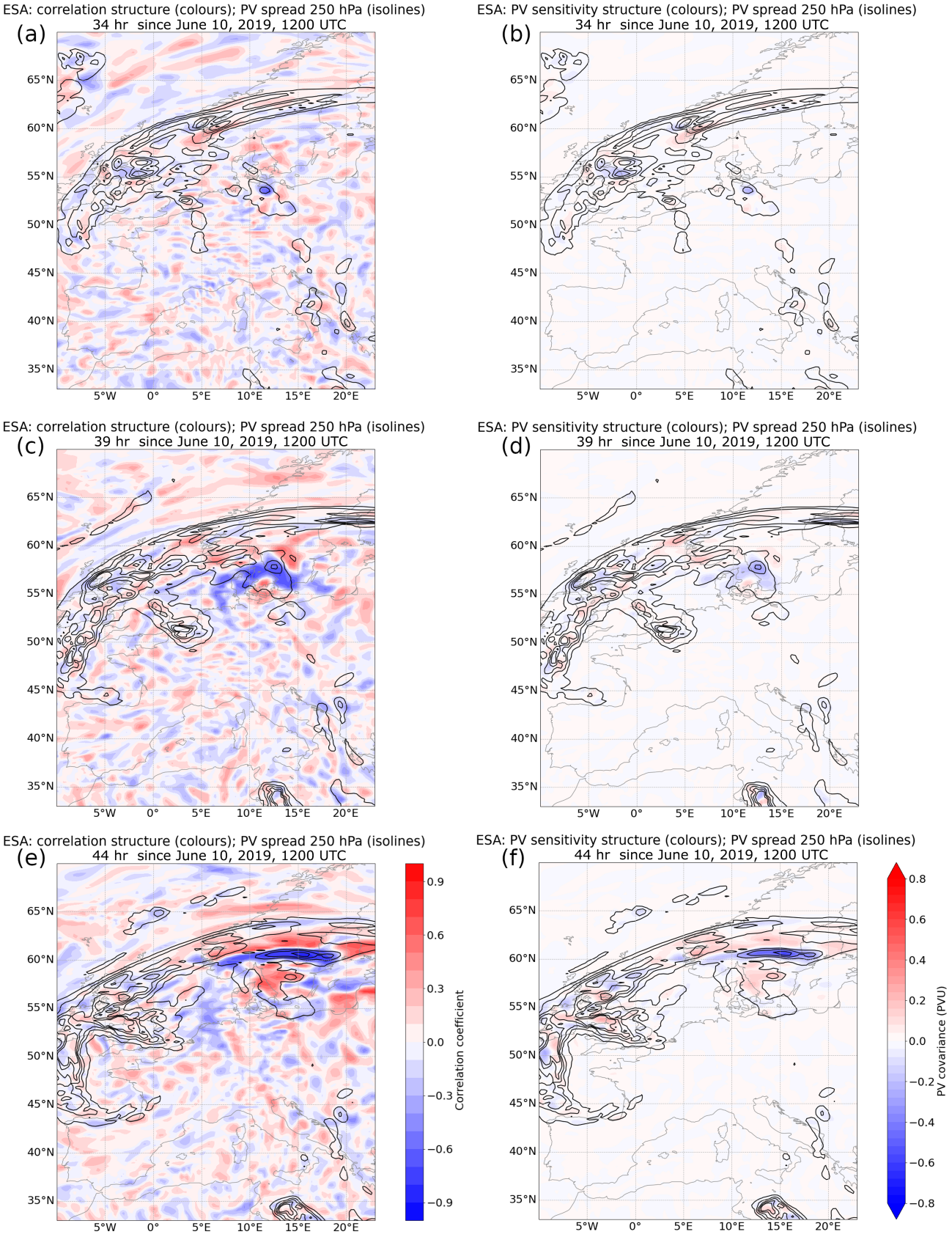

FIGURE 8 Ensemble sensitivity of the potential vorticity (PV) at 250 hPa with respect to the mass divergence over the region of the Baltic Sea convective system, 34–37 hr. The correlation structure is shown on the left and the PV amplitude on the right: (a, b) 34 hr; (c, d) 39 hr; (e, f) 44 hr. Contours show the PV spread within the ensemble at 0.16 PVU intervals. ESA: ensemble sensitivity analysis. [Colour figure can be viewed at wileyonlinelibrary.com]

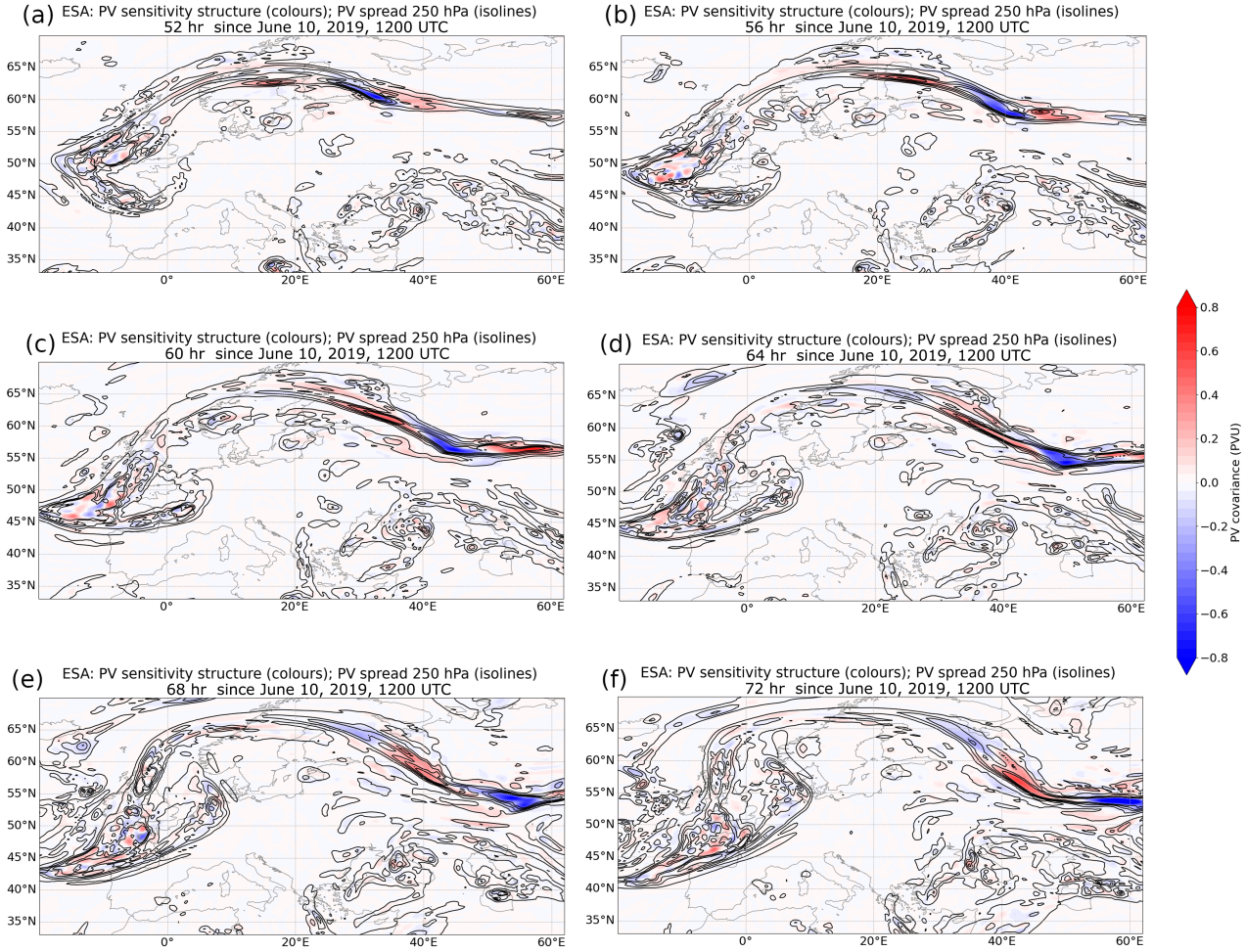

FIGURE 9 Potential vorticity (PV) co-variance associated with the mass divergence after 34–37 hr over the Baltic Sea system's box volume for every 4 hr on the third simulation day. Contours show 250 hPa PV spread within the ensemble at 0.16 PVU intervals. ESA: ensemble sensitivity analysis. [Colour figure can be viewed at wileyonlinelibrary.com]

difference to the large-scale jet structure. During day 2, the jet exhibited a largely zonal orientation downstream of the Germany system, whereas on day 3 an eminent large-scale wave pattern develops. The larger wave amplitude implies a higher degree of nonlinearity in the underlying dynamics on day 3—a prerequisite for spread amplification by rotational tendencies (Baumgart *et al.*, 2018). Thereby, "local" spread growth associated with the Baltic Sea system exhibits the characteristics of three-stage spread growth as indicated in the average sense (over large regions and many cases) by Baumgart *et al.* (2019) and Selz *et al.* (2022).

4.4 | Connection between convective variability and long-wave radiation tendencies

Near the midlatitude tropopause, PV tendencies associated with long-wave radiation are on average the dominant nonconservative PV tendencies (Teubler & Riemer, 2021) (in the stages where the advective tendencies dominate). To a large part, however, these tendencies exhibit relatively small spatial and temporal variation, such that it was proposed that only a small fraction of these tendencies may impact on the synpotic- or smaller-scale dynamics (Teubler & Riemer, 2021). In the context of an idealised life cycle, Keshtgar *et al.* (2023) demonstrated that cloud-radiative heating exerts systematic differences on the evolution of cyclones, which propagate upscale following the sequence of mechanisms identified by Baumgart *et al.* (2019). In previous spread-growth experiments that considered spread-growth mechanisms averaged over large spatial regions and many cases, however, long-wave radiation did not receive particular attention as a major spread-growth mechanism (Baumgart *et al.*, 2019; Selz *et al.*, 2022). Here, our case-specific analysis reveals that long-wave radiation may be about as dominant as, or locally in space and time even more dominant (at tropopause levels) than, direct convective heating tendencies. This subsection therefore examines,

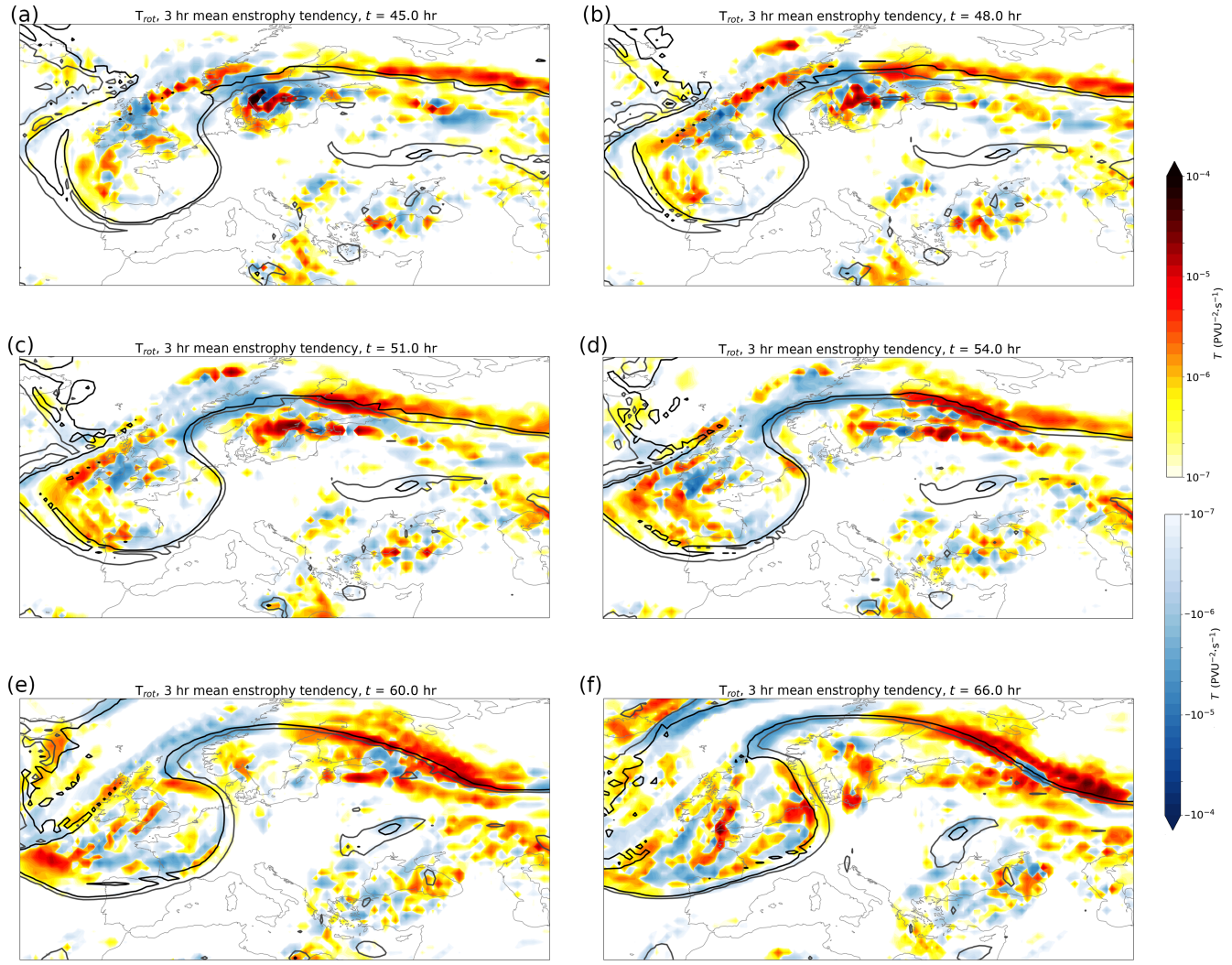

FIGURE 10 The 3 hr mean of the potential enstrophy tendency as a result of differential advection by the rotational wind, at θ of 327.5–335 K: $t = 45$, $t = 48$, $t = 51$, $t = 54$, $t = 60$ and $t = 66$ hr. Red colours indicate spread growth, whereas blue colours indicate spread reduction. For this level, the dynamical tropopause (2 PVU) and 4 PVU contour are also shown in dark grey/black. [Colour figure can be viewed at wileyonlinelibrary.com]

to our knowledge for the first time, spread growth due to long-wave radiation in some more depth. Before proceeding, it should be noted that the tendencies are expected to magnify whenever anvils with strong (differential) radiation tendencies affect the tropopause, consistent with the analyses of Teubler and Riemer (2021) and Keshtgar *et al.* (2023). However, updraughts of not all convective systems penetrate the upper troposphere and tropopause, such that differential long-wave heating at these levels only occurs in some convective systems (and with widely varying spatial mean heating rates). Mesoscale convective systems are comparatively likely to produce strong mean long-wave heating rates among all convective systems.

Figure 11 shows the temperature tendencies originating from the long-wave radiation parametrisation over the region of the convective system in northern Germany after 38 hr. It shows that there is some connection between the temperature tendencies at anvil level (model levels 48–51; near-tropopause, 200 hPa) and the precipitation rate (35–38 hr). The intenser the convective precipitation is, the larger the mean temperature tendencies tend to get at the anvil (especially at level 50). When we look further down at levels 55–59 (between 250 and 300 hPa), the pattern is reversed.

It is important to realise that the effect of these heating tendencies onto PV spread growth mostly derives from variability in "vertical gradients" of potential temperature tendencies. The slightly amplified vertical gradient in Figure 11 hence suggests amplified negative PV perturbations stemming from long-wave tendencies just below anvil level, at model levels 51–53 in all members and by extension levels 49–54 in some members (an overlap with

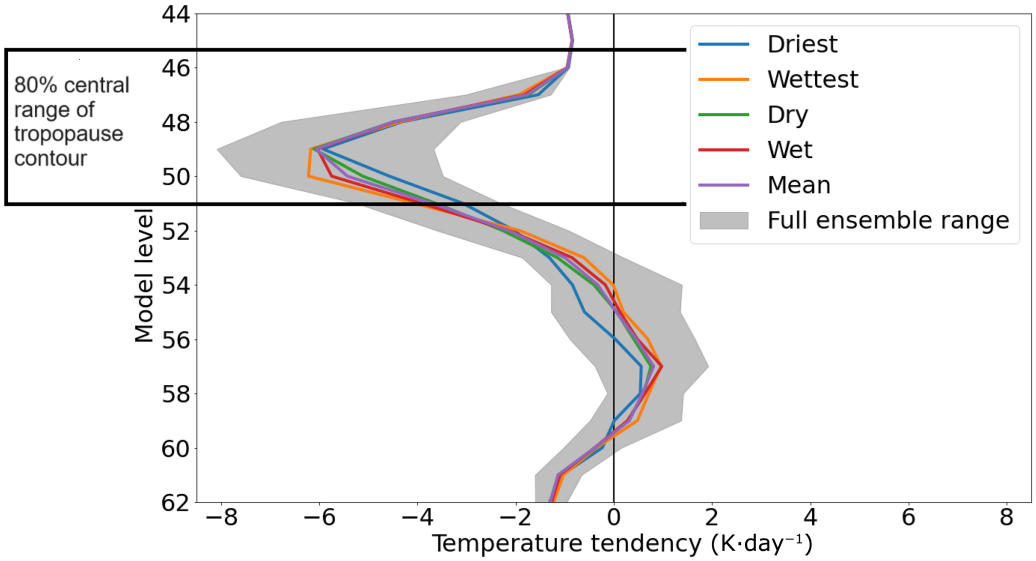

FIGURE 11 Temperature tendency from long-wave radiation as a function of model level over the upper troposphere (covering the vertical range from 150 to 450 hPa), after 37.5–38.0 hr in the convective system over northern Germany. Highlighted are also the model levels at which the dynamical tropopause (2 PVU) is located over the corresponding region. Next to the area and ensemble mean, the area means over the driest (10–14%), dry (35–39%), wet (35–39%), and wettest (10–14%) ensemble members are shown, which is based on mean precipitation rate over the 35–38 hr time interval. The outer boundary of the grey shading corresponds to ensemble maximum (minimum) of long-wave temperature tendencies during the same interval. [Colour figure can be viewed at wileyonlinelibrary.com]

the dynamical tropopause). On the contrary, in all members, (weak) positive perturbations will occur near level 60 and (stronger) near level 47. On the one hand, the rough scaling of the heating gradient at levels 50–53 with precipitation rate and, on the other hand, subtle vertical shifts of cooling/heating could, together, likely explain the strong tendencies originating from long-wave radiation in the tendency diagnostics, at least to some extent.

Interestingly, a comparison of the tendencies between 35–36 and 38 hr suggests that a more elevated overshoot in the Baltic Sea convective system at model levels 48–49 tends to be associated with the wet and wettest ensemble members. Furthermore, this relation between the area mean vertical long-wave radiative heating gradient at these levels and the precipitation rate shows that the convective variability (both precipitation rates and outflow rates) are linked with long-wave radiation tendencies. Therefore, convective variability has the potential to not only trigger PV-spread tendencies induced by the convective parametrisation, but also by differences in long-wave radiation.

Although our experiment has not been designed to target extensive analysis of long-wave radiation, our analysis reveals an interesting and close link between long-wave radiative heating variability and variability in the mesoscale convective system on day 2 of our experiments, which has been shown to affect spread growth. Therefore, further investigations of case to case variability in long-wave and convective heating tendencies near the intrinsic limit would be beneficial to understand the link of long-wave spread tendencies to convective variability and spread-growth stages better, ideally with refined resolution in the upper troposphere and lower stratosphere.

5 | SUMMARY AND DISCUSSION

We investigate spread growth in an ICON ensemble experiment initialised with miniscule initial-condition uncertainty (rescaled to 0.1% of a typical current-day operational level). The experiment covers a 3-day period in summer, when three mesoscale convective systems develop over Europe in the vicinity of the midlatitude jet. Even in this set-up near the intrinsic limit of predictability, one of the convective systems substantially affects the synoptic-scale flow about 1 day after its convective initiation. Variability in the jet location of ≈100 km is associated with variability of upper tropospheric divergence and, correspondingly, 3–4% uncertainty in precipitation rates of this system. Precipitation variability in an operational ensemble is currently larger by about an order of magnitude. Consequently, for (almost) any realistic forecast, convective uncertainty amplifies spread growth very rapidly, whereby stage 3 of spread growth (typically) dominates immediately in an ensemble (see also Selz *et al.*, 2022). Therefore, even without regime transition in the dominant spread growth dynamics from stages 1 to 3, enhanced precipitation variability within realistic ensembles would likely

permit much larger jet stream uncertainty at short lead times.

The focus of the study is on the analysis of the conceptual three-stage sequence of dominant spread-growth mechanisms, previously identified from a statistically averaged perspective by Baumgart *et al.* (2019); Selz *et al.* (2022); that is, as composite evolution over many cases and very large regions. More specifically, the key question of this study is whether we can identify the same three-stage sequence "locally"; that is, in the spread evolution originating from specific convective systems.

5.1 | Stages of spread growth

The spread evolution originating from the individual convective systems exhibits some commonalities, but also distinct differences. The commonalities can be summarised as follows. Convective PV-spread tendencies dominate spread growth in the initial stages of the convective systems, which can be expected due to the design of the experiment. Long-wave radiative-spread tendencies become equally or even more important in the convective region (and partly downstream) a few hours later. The upper tropospheric divergent flow amplifies spread in the vicinity of the convective systems, and all systems interact with the strong PV gradient associated with the jet.

Only one of the three convective systems (the Baltic Sea system) exhibits the full signature of the previously identified three-stage sequence. After initial growth of spread, which is dominated by convection, variability in the divergent outflow from the Baltic Sea system interacts with the jet and dominates amplification of PV spread along the strong PV gradient in the interaction region. Subsequently, the spread pattern propagates downstream and can unambiguously be traced by (linear) ESA. Spread amplification in the downstream region is dominated by nonlinear growth, as indicated by rotational tendencies aligned with the strong PV gradient.

For another convective system (the Germany system), divergent tendencies also dominate after an initial convective stage. In contrast to the Baltic Sea system, however, the associated spread amplification occurs locally above the convective system, arguably associated with the adjustment of convective outflow to a balanced, anticyclonic flow component, rather than in direct interaction with the jet. Subsequently, an interaction of this anticyclone with the jet is indicated by rotational tendencies along the strong PV gradient. This evolution is thereby consistent with the second stage of the conceptual model proposed by Zhang *et al.* (2007), which assumes that a general adjustment-to-balance process occurs after a first stage of convective spread growth (and before a third stage of growth on geostrophically balanced scales). In our case, however, this interaction with the jet stream is not followed by substantial jet variability in the associated region downstream.

For the third system, the Alps system, both PV-spread tendencies and ESA indicate an interaction of convective outflow with the jet. Subsequent nonlinear growth is indicated by rotational tendencies. However, neither of these two processes dominates spread growth for any period of time. Neither distinct stages of spread growth can thus be identified after the initial convective growth nor a persistent coherent downstream sensitivity with respect to the system's outflow.

In addition to the spread-growth mechanisms emphasised in the previous multistage conceptual models by Zhang *et al.* (2007) and Baumgart *et al.* (2019), we find that long-wave radiative tendencies make a considerable contribution to spread amplification in the vicinity of convective systems. Briefly after the start of the first convective stage of spread growth, long-wave radiative tendencies become comparable to or even larger than convective tendencies. Importantly, long-wave radiative tendencies can outlive convective tendencies and extend over larger regions, arguably associated with the anvils of the convective systems. Though a considerable contribution by long-wave radiative tendencies has been documented as an aside previously (e.g., Baumgart *et al.*, 2019; Selz *et al.*, 2022), we here demonstrate explicitly that variability of long-wave radiative tendencies in one of our convective systems is associated with local convective variability. In this sense, long-wave radiative tendencies communicate convective variability to the tropopause region and can be thereby considered as an inherent contribution to the convective stage of spread growth. Moreover, by extending over larger regions, long-wave radiative tendencies arguably contribute to an upscale impact of convective variability, complementing the role of the convective tendencies in the first stage and divergent wind in a second conceptual stage of spread growth.

On the one hand, substantial divergent tendencies appear very early (before 12 hr)—consistent with Zhang *et al.* (2007); Baumgart *et al.* (2019)—indicating an onset of stage 2 at the PV gradient near the Alps system. On the other hand, however, another region becomes saturated with convective and long-wave tendencies at 36 hr, which follows on an episode with little spread, indicating that stage 1 is locally reinitiated much later. For both systems, the initiation of stage 1 is rapidly followed by the onset of stage 2 and by rotational spread tendencies (conceptually indicating the onset of stage 3). The rotational tendencies of the conceptually exemplary Baltic Sea system appear after about 12 hr of stage 1 and, subsequently, stage 2 spread growth (at about 48 hr; Figure 10b). The variation

in the timing of the onset of stage 1, followed by a rapid transition to subsequent stages, contrasts estimates from the mean perspective and certainly indicates substantial variation in spread-growth stages locally. From the mean perspective, variability cannot be determined easily. The differences may be explained by temporal variability in the development of rapidly spread-saturated areas at larger mesoscales; convective initiation occurs at random times and, subsequently, convective-scale spread can saturate in a couple of hours (e.g. Groot & Tost, 2023a; Hohenegger & Schar, 2007; Weyn & Durran, 2017) in regions of active convection. Thereby, spread-prone regions may locally project spread on jet streams quickly and feed larger scale spread (like the Baltic Sea system). Finally, few of the mesoscale convective systems in proximity of the jet stream likely associate with lagged downstream jet variability (and hence traces of their variability likely decay); that is, spread evolves rarely across all three conceptual stages (whether it does may incidentally be probabilistic; e.g., Lorenz, 1969; Melhauser & Zhang, 2012)).

A key question that our results imply is what governs the observed variability in the characteristics of the presumed second and third stages. Based on a case study of merely three convective systems, we can provide a preliminary answer at best. We attribute the lack of spread growth during the presumed occurrence of third-stage spread-growth dynamics associated with the Germany system to the jet structure in the downstream region. The associated strong PV gradient approximately exhibits a zonal orientation, which can be expected to support a linear evolution of (small) perturbations to the jet. Nonlinear dynamics, however, are required for spread to amplify due to rotational tendencies along a jet (Baumgart *et al.*, 2018). Consistently, third-stage spread growth due to rotational tendencies is observed downstream of the Baltic Sea system in a higher-amplitude wave pattern. For the Alps system, the upstream trough is undergoing rapid wave breaking. Arguably, this wave breaking prohibits the coherent downstream propagation and amplification of spread along the jet. Moreover, spread tendencies that are not related to the Alps system (associated with a weather system over the United Kingdom and the North Sea; not discussed in detail in Section 4) arguably complicate the attribution of the spread evolution within the trough to the Alps system.

An explanation for the observed variability in the presumed second stage of spread growth is more elusive. To our knowledge, the linear, time-dependent analytical model for geostrophic adjustment and its application to idealised experiments of upscale growth by Shutts and Gray (1994); Bierdel *et al.* (2017, 2018) provides the most comprehensive theoretical framework for upscale growth during a presumed second stage. Though the model generally confirms the hypothesis by Zhang *et al.* (2007) that geostrophic adjustment is a viable mechanism for upscale growth, the model does not consider the existence of strong, localised PV gradients, and thereby it is not clear how the model could be applied to investigate the flow dependence of geostrophic adjustment in the vicinity of a jet. In our experiment, the differences between the Germany system and the Baltic Sea system may relate to differences in the distance of the convective system to the jet (arguably relative to the local deformation radius, which is an upper bound to the scale of geostrophic adjustment). Regarding the Alps system, we may speculate that the lack of a distinct second stage relates to the alignment of the interaction between the convective variability and the jet within the wave phase of the midlatitude wave. The Alps system interacts with the upstream trough, whereas spread growth due to divergent outflow from the other two systems occurs within the downstream ridge. The downstream impact of recurving tropical cyclones has been shown to depend sensitively on the relative position of recurvature with respect to the midlatitude wave pattern (Keller *et al.*, 2019). To the extent that this result may transfer to mesoscale convective systems, we could hypothesise that spread growth due to convective uncertainty depends on the "phase relation" between convective systems and the midlatitude wave pattern, and not only on distance. Clearly, further research into the dynamical constraints under which the second and third stages are favoured (or, conversely, restricted) is needed to verify our rather speculative explanations.

5.2 | Reflection on the experimental design and outlook

We find that spread evolution may be interpreted more robustly under some conditions when spread tendency diagnostics are complemented with a linear sensitivity analysis. By combining the tools, the quantitative impact of a precursor on spread downstream is established. Here, about half the local downstream jet stream variability at 60 hr relates to the Baltic Sea system's outflow. Though linear analysis does not allow one to robustly quantify statistical connections with substantial nonlinearity, we utilise the improved tractability of convective variability by combining careful experimental design with knowledge of the close association between outflow and convective heating (Groot *et al.*, 2024).

In a convection-permitting configuration, the downstream impact of outflows of organised convection can be traced in more detail because the representation of these outflows is refined in high-resolution simulations (Groot, 2023; Groot *et al.*, 2024; Groot & Tost, 2023b). In

such simulations, the outflow can be understood conceptually as a combination of two components: (a) a contribution linearly dependent on latent heating and (b) an approximately multiplicative component resulting from convective organisation or geometry. Nonetheless, from a practical point of view, this will first require a development to track each of the aforementioned two components of outflow variability, which would require a robust quantitative tracking framework—this needs further investigation, following Groot *et al.* (2024). Nonlinear (multiplicative) effects reduce the tractability of convective variability downstream when both components are represented (i.e., at high resolution). Furthermore, both effects are time dependent in real systems. Consequently, it is likely difficult to track nonlinear variability associated with outflow variability in convection-permitting configurations.

The negligence of the multiplicative nature and other nonlinear aspects of mesoscale convective system variability growth may affect current uncertainty evolution in state-of-the-art numerical weather prediction ((e.g., through incompletely addressing convective initiation; Melhauser & Zhang, 2012; Groot & Tost, 2023a), which may be associated with interactions with subgrid gravity waves, microphysics tendencies, and advection). The largely linear nature of downstream jet evolution with respect to outflow rate we diagnose at scales of ≈500 km may imply that our numerical weather prediction models describe mesoscale convective systems in a too simple way – at least when convection is not explicitly resolved. This would possibly lead to slightly optimistic estimates of the predictability horizon at the mesoscales, although it is well-known that mesoscales play an apparently limited role as a source of overall predictability to larger scales (e.g., Lorenz, 1969; Selz *et al.*, 2022; Zhang *et al.*, 2019). This would be a strong reason for further studies of the limits of predictability to utilise convection-permitting configurations, especially if convection is important and the aim of a study is to also assess the details of interactions at mesoscales.

In real forecasting applications, the implications of nonlinear aspects of mesoscale convective system variability are simulated by applying complementary stochastic schemes to amplify error growth from parametrisation—for a more elaborate discussion, see Leutbecher *et al.* (2017) and (Groot, 2023, chap. 7)—although the immediate excitation of barotropic uncertainty growth probably overwhelms physics-induced uncertainty growth in (nearly) all real ensemble forecasting (Baumgart *et al.*, 2019; Selz *et al.*, 2022).

Groot *et al.* (2024) have shown that grid spacing affects the representation of divergent outflows, differing between convection-permitting 1 km grid and convection-parametrising 13 km grid configurations of ICON. Here, the near-linear response of divergent outflows in parametrised convection allows us to effectively track the role of the convective variability (and tendencies) downstream. Accordingly, by investigating a configuration with near-linear response, convective variability and divergence are tightly related. Future experiments could aim to identify propagation of individual wave signals, as associated with convective outflows, and attribute the waves to divergent winds. Thereby, a wavelet analysis of the winds, and possibly even spread tendencies, could be utilised to further establish their connection, although this may be very challenging from a practical perspective. Furthermore, it will be worthwhile to examine the co-variability of convective activity and long-wave radiative tendencies in further quantitative and qualitative detail in future work. Finally, we think that further understanding of case-to-case variability of spread growth during the presumed second and third stages is a particularly fruitful avenue for future research, especially if we can constrain dynamical conditions favouring strong spread growth. Investigating the second stage, which implies the upscale impact of convection, can be expected to specifically benefit from using convection-permitting experiments.

ACKNOWLEDGEMENTS

We would like to thank Tobias Selz, Holger Tost, and George Craig for their feedback on the initial idea for this study and for the joint discussions within the A1 project. Furthermore, we would like to thank Tobias Selz for providing further technical support; for example, by providing case-specific initial conditions following Selz *et al.* (2022), providing access to the associated code, and suggestions to improve the work.

We would also like to acknowledge the computing time granted on the supercomputer MOGON 2 at Johannes Gutenberg-University Mainz (hpc.uni-mainz.de; last accessed: February 12, 2025) and Wavestoweather's computational infrastucture.

FUNDING INFORMATION

The research leading to these results has been done within the subproject "A1 – Multiscale analysis of the evolution of forecast uncertainty" of the Transregional Collaborative Research Center SFB/TRR 165 "Waves to Weather" funded by the German Research Foundation (DFG). EG acknowledges additional funding at the Leverhulme Trust grant funds EG's current position at the University of Oxford. In addition, both authors acknowledge TRR-165 'WavestoWeather' by the German Research Foundation (DFG) (RPG-2022-192).

CONFLICT OF INTEREST STATEMENT

The authors declare that they are not aware of any conflict of interest.

DATA AVAILABILITY STATEMENT

The data that support the findings of this study are openly available in dataset of "When tiny convective spread affects a midlatitude jet: Spread sequence" at https://doi.org/10.5281/zenodo.14861019, reference number 10.5281/zenodo.14861019.

ORCID

Edward Groot https://orcid.org/0000-0002-7098-2383

REFERENCES

Ancell, B.C. & Hakim, G.J. (2007) Comparing adjoint and ensemble sensitivity analysis. *Monthly Weather Review*, 135, 4117–4134.

Anwender, D., Harr, P.A. & Jones, S.C. (2008) Predictability associated with the downstream impacts of the extratropical transition of tropical cyclones: case studies. *Monthly Weather Review*, 136(9), 3226–3247.

Baumgart, M., Ghinassi, P., Wirth, V., Selz, T., Craig, G.C. & Riemer, M. (2019) Quantitative view on the processes governing the upscale error growth up to the planetary scale using a stochastic convection scheme. *Monthly Weather Review*, 147(5), 1713–1731. Available from: https://doi.org/10.1175/mwr-d-18-0292.1

Baumgart, M. & Riemer, M. (2019) Processes governing the amplification of ensemble spread in a medium-range forecast with large forecast uncertainty. *Quarterly Journal of the Royal Meteorological Society*, 145(724), 3252–3270.

Baumgart, M., Riemer, M., Wirth, V., Teubler, F. & Lang, S.T.K. (2018) Potential vorticity dynamics of forecast errors: a quantitative case study. *Monthly Weather Review*, 146(5), 1405–1425. Available from: https://doi.org/10.1175/MWR-D-17-0196.1

Bechtold, P., Semane, N., Lopez, P., Chaboureau, J.P., Beljaars, A. & Bormann, N. (2014) Representing equilibrium and nonequilibrium convection in large-scale models. *Journal of the Atmospheric Sciences*, 71(2), 734–753.

Bednarczyk, C.N. & Ancell, B.C. (2015) Ensemble sensitivity analysis applied to a southern plains convective event. *Monthly Weather Review*, 143(1), 230–249. Available from: https://doi.org/10.1175/MWR-D-13-00321.1

Bierdel, L., Selz, T. & Craig, G.C. (2017) Theoretical aspects of upscale error growth through the mesoscales: an analytical model. *Quarterly Journal of the Royal Meteorological Society*, 143(709), 3048–3059. Available from: https://doi.org/10.1002/qj.3160.

Bierdel, L., Selz, T. & Craig, G.C. (2018) Theoretical aspects of upscale error growth on the mesoscales: Idealized numerical simulations. *Quarterly Journal of the Royal Meteorological Society*, 144(712), 682–694. Available from: https://doi.org/10.1002/qj.3236.

Binder, H., Rivière, G., Arbogast, P., Maynard, K., Bosser, P., Joly, B. et al. (2021) Dynamics of forecast-error growth along cut-off s anchez and its consequence for the prediction of a high-impact weather event over southern France. *Quarterly Journal of the Royal Meteorological Society*, 147(739), 3263–3285.

Bretherton, C.S. & Smolarkiewicz, P.K. (1989) Gravity waves, compensating subsidence and detrainment around cumulus clouds. *Journal of the Atmospheric Sciences*, 46(6), 740–759. Available from: https://doi.org/10.1175/1520-0469(1989)046<0740:GWCSAD>2.0.CO;2

Chagnon, J.M. & Gray, S.L. (2009) Horizontal potential vorticity dipoles on the convective storm scale. *Quarterly Journal of the Royal Meteorological Society*, 135(643), 1392–1408.

Clarke, S.J., Gray, S.L. & Roberts, N.M. (2019a) Downstream influence of mesoscale convective systems. Part 1: influence on forecast evolution. *Quarterly Journal of the Royal Meteorological Society*, 145(724), 2933–2952. Available from: https://doi.org/10.1002/qj.3593

Clarke, S.J., Gray, S.L. & Roberts, N.M. (2019b) Downstream influence of mesoscale convective systems. Part 2: influence on ensemble forecast skill and spread. *Quarterly Journal of the Royal Meteorological Society*, 145(724), 2953–2972. Available from: https://doi.org/10.1002/qj.3613

Davies, H.C. & Didone, M. (2013) Diagnosis and dynamics of forecast error growth. *Monthly Weather Review*, 141(7), 2483–2501.

Davis, C.A., Grell, E.D. & Shapiro, M.A. (1996) The balanced dynamical nature of a rapidly intensifying oceanic cyclone. *Monthly Weather Review*, 124(1), 3–26.

Dawson, A., Irving, D., T. Edwards, Comer, R., Filipe, R. & Russo, A. (2018) *ajdawson/windspharm: version 1.7.0*. https://doi.org/10.5281/zenodo.1401190

Done, J.M., Craig, G.C., Gray, S.L., Clark, P.A. & Gray, M.E.B. (2006) Mesoscale simulations of organized convection: importance of convective equilibrium. *Quarterly Journal of the Royal Meteorological Society*, 132(616), 737–756.

Durran, D.R. & Gingrich, M. (2014) Atmospheric predictability: why butterflies are not of practical importance. *Journal of the Atmospheric Sciences*, 71(7), 2476–2488. Available from: https://doi.org/10.1175/JAS-D-14-0007.1

Ertel, H. (1942) Ein neuer hydrofynamischer wirbelsatz. *Meteorologische Zeitschrift*, 59, 277–282.

Giorgetta, M.A., Brokopf, R., Crueger, T., Esch, M., Fiedler, S., Helmert, J. et al. (2018) ICON-A, the atmosphere component of the ICON earth system model: I. model description. *Journal of Advances in Modeling Earth Systems*, 10(7), 1613–1637.

Grams, C.M., Wernli, H., Böttcher, M., Čampa, J., Corsmeier, U., Jones, S.C. et al. (2011) The key role of diabatic processes in modifying the upper-tropospheric wave guide: a north atlantic case-study. *Quarterly Journal of the Royal Meteorological Society*, 137(661), 2174–2193.

Groot, E. (2023) *An analysis of variability and predictability of organised deep convection and its divergent upper tropospheric outflow*. PhD thesis, Johannes Gutenberg University.

Groot, E., Kuntze, P., Miltenberger, A. & Tost, H. (2024) Divergent convective outflow in icon deep-convection-permitting and parameterised deep convection simulations. *Weather and Climate Dynamics*, 5(2), 779–803.

Groot, E. & Tost, H. (2023a) Evolution of squall line variability and error growth in an ensemble of large eddy simulations. *Atmospheric Physics and Chemistry*, 23, 565–585. Available from: https://doi.org/10.5194/acp-23-565-2023

Groot, E. & Tost, H. (2023b) Divergent convective outflow in large-eddy simulations. *Atmospheric Chemistry and Physics*, 23, 6065–6081. Available from: https://doi.org/10.5194/acp-23-6065-2023

Hanley, K.E., Kirshbaum, D.J., Roberts, N.M. & Leoncini, G. (2013) Sensitivities of a squall line over Central Europe in a convective-scale ensemble. *Monthly Weather Review*, 141(1), 112–133. Available from: https://doi.org/10.1175/MWR-D-12-00013.1

Hohenegger, C. & Schar, C. (2007) Atmospheric predictability at synoptic versus cloud-resolving scales. *Bulletin of the American Meteorological Society*, 88(11), 1783–1794.

Judt, F. (2018) Insights into atmospheric predictability through global convection-permitting model simulations. *Journal of the Atmospheric Sciences*, 75(5), 1477–1497. Available from: https://doi.org/10.1175/JAS-D-17-0343.1

Keller, J.H., Grams, C.M., Riemer, M., Archambault, H.M., Bosart, L., Doyle, J.D. et al. (2019) The extratropical transition of tropical cyclones. Part II: interaction with the midlatitude flow, downstream impacts, and implications for predictability. *Monthly Weather Review*, 147(4), 1077–1106.

Keshtgar, B., Voigt, A., Hoose, C., Riemer, M. & Mayer, B. (2023) Cloud-radiative impact on the dynamics and predictability of an idealized extratropical cyclone. *Weather and Climate Dynamics*, 4(1), 115–132. Available from: https://doi.org/10.5194/wcd-4-115-2023

Leutbecher, M., Lock, S.J., Ollinaho, P., Lang, S.T.K., Balsamo, G., Bechtold, P. et al. (2017) Stochastic representations of model uncertainties at ECMWF: state of the art and future vision. *Quarterly Journal of the Royal Meteorological Society*, 143(707), 2315–2339. Available from: https://doi.org/10.1002/qj.3094

Lojko, A., Payne, A. & Jablonowski, C. (2022) The remote role of north-American mesoscale convective systems on the forecast of a Rossby wave packet: a multi-model ensemble case-study. *Journal of Geophysical Research: Atmospheres*, 127(24), e2022JD037171. Available from: https://doi.org/10.1029/2022JD037171

Lorenz, E.N. (1969) The predictability of a flow which possesses many scales of motion. *Tellus*, 21(3), 289–307. Available from: https://doi.org/10.3402/tellusa.v21i3.10086

Magnusson, L. (2017) Diagnostic methods for understanding the origin of forecast errors. *Quarterly Journal of the Royal Meteorological Society*, 143(706), 2129–2142.

Mapes, B.E. (1993) Gregarious tropical convection. *Journal of the Atmospheric Sciences*, 50(13), 2026–2037. Available from: https://doi.org/10.1175/1520-0469(1993)050<2026:GTC>2.0.CO;2

Melhauser, C. & Zhang, F. (2012) Practical and intrinsic predictability of severe and convective weather at the mesoscales. *Journal of the Atmospheric Sciences*, 69(11), 3350–3371. Available from: https://doi.org/10.1175/jas-d-11-0315.1

Nicholls, M.E., Pielke, R.A. & Cotton, W.R. (1991) Thermally forced gravity waves in an atmosphere at rest. *Journal of the Atmospheric Sciences*, 48(16), 1869–1884. Available from: https://doi.org/10.1175/1520-0469(1991)048<1869:TFGWIA>2.0.CO;2

Palmer, T.N., Döring, A. & Seregin, G. (2014) The real butterfly effect. *Nonlinearity*, 27(9), R123–R141. Available from: https://doi.org/10.1088/0951-7715/27/9/R123

Parsons, D.B., Lillo, S.P., Rattray, C.P., Bechtold, P., Rodwell, M.J. & Bruce, C.M. (2019) The role of continental mesoscale convective systems in forecast busts within global weather prediction systems. *Atmosphere*, 10(11), 681.

Plant, R.S. & Craig, G.C. (2008) A stochastic parameterization for deep convection based on equilibrium statistics. *Journal of the Atmospheric Sciences*, 65(1), 87–105. Available from: https://doi.org/10.1175/2007JAS2263.1

Prill, F., Reinert, D., Rieger, D., Zängl, G., Schröter, J., Örstner, J. et al. *ICON model tutorial 2019*, 2019. https://www.dwd.de/DE/leistungen/nwv_icon_tutorial/pdf_einzelbaende/icon_tutorial2020.pdf.

Riemer, M., Jones, S.C. & Davis, C.A. (2008) The impact of extratropical transition on the downstream flow: an idealized modelling study with a straight jet. *Quarterly Journal of the Royal Meteorological Society*, 134(630), 69–91. Available from: https://doi.org/10.1002/qj.189

Rodwell, M.J., Magnusson, L., Bauer, P., Bechtold, P., Bonavita, M., Carla, C. et al. (2013) Characteristics of occasional poor medium-range weather forecasts for Europe. *Bulletin of the American Meteorological Society*, 94(9), 1393–1405. Available from: https://doi.org/10.1175/bams-d-12-00099.1

Schmidt, S., Riemer, M., De Heuvel, J., McTaggart-Cowan, R. & Selz, T. (2025) A feature-based framework to investigate atmospheric predictability. *Monthly Weather Review*, 153, 1431–1450. Available from: https://doi.org/10.1175/MWR-D-24-0090.1.

Schulzweida, U. (2022) *Cdo user guide*. https://doi.org/10.5281/zenodo.7112925

Seifert, A. (2008) A revised cloud microphysical parameterization for COSMO-LME. *COSMO Newsletter*, 7, 25–28.

Selz, T. (2019) Estimating the intrinsic limit of predictability using a stochastic convection scheme. *Journal of the Atmospheric Sciences*, 76(3), 757–765. Available from: https://doi.org/10.1175/jas-d-17-0373.1

Selz, T. & Craig, G.C. (2015) Upscale error growth in a high-resolution simulation of a summertime weather event over Europe. *Monthly Weather Review*, 143(3), 813–827. Available from: https://doi.org/10.1175/mwr-d-14-00140.1

Selz, T., Riemer, M. & Craig, G.C. (2022) The transition from practical to intrinsic predictability of midlatitude weather. *Journal of the Atmospheric Sciences*, 79(8), 2013–2030. Available from: https://doi.org/10.1175/JAS-D-21-0271.1

Shutts, G. (2017) Idealized numerical simulations of mesoscale convective systems and their implications for forecast error. *Quarterly Journal of the Royal Meteorological Society*, 143(704), 1608–1619. Available from: https://doi.org/10.1002/qj.3031

Shutts, G.J. & Gray, M.E.B. (1994) A numerical modelling study of the geostrophic adjustment process following deep convection. *Quarterly Journal of the Royal Meteorological Society*, 120(519), 1145–1178.

Sun, Y.Q. & Zhang, F. (2016) Intrinsic versus practical limits of atmospheric predictability and the significance of the butterfly effect. *Journal of the Atmospheric Sciences*, 73(3), 1419–1438. Available from: https://doi.org/10.1175/JAS-D-15-0142.1

Teubler, F. & Riemer, M. (2021) Potential-vorticity dynamics of troughs and ridges within rossby wave packets during a 40-year reanalysis period. *Weather and Climate Dynamics*, 2(3), 535–559. Available from: https://doi.org/10.5194/wcd-2-535-2021

Tiedtke, M. (1989) A comprehensive mass flux scheme for cumulus parameterization in large-scale models. *Monthly Weather Review*, 117(8), 1779–1800.

Torn, R.D. & Hakim, G.J. (2008) Ensemble-based sensitivity analysis. *Monthly Weather Review*, 136(2), 663–677.

Torn, R.D. & Romine, G.S. (2015) Sensitivity of Central Oklahoma convection forecasts to upstream potential vorticity anomalies during two strongly forced cases during MPEX. *Monthly Weather*

Review, 143(10), 4064–4087. Available from: https://doi.org/10.1175/MWR-D-15-0085.1

Weijenborg, C., Chagnon, J.M., Friederichs, P., Gray, S.L. & Hense, A. (2017) Coherent evolution of potential vorticity anomalies associated with deep moist convection. *Quarterly Journal of the Royal Meteorological Society*, 143(704), 1254–1267. Available from: https://doi.org/10.1002/qj.3000

Weijenborg, C., Friederichs, P. & Hense, A. (2015) Organisation of potential vorticity on the mesoscale during deep moist convection. *Tellus A: Dynamic Meteorology and Oceanography*, 67(1), 25705.

Weyn, J.A. & Durran, D.R. (2017) The dependence of the predictability of mesoscale convective systems on the horizontal scale and amplitude of initial errors in idealized simulations. *Journal of the Atmospheric Sciences*, 74(7), 2191–2210. Available from: https://doi.org/10.1175/JAS-D-17-0006.1

Wilhelm, J., Mohr, S., Punge, H.J., Mühr, B., Schmidberger, M., Daniell, J.E. et al. (2021) Severe thunderstorms with large hail across Germany in June 2019. *Weather*, 76(7), 228–237. Available from: https://doi.org/10.1002/wea.3886

Zängl, G., Reinert, D., Rípodas, P. & Baldauf, M. (2015) The ICON (ICOsahedral non-hydrostatic) modelling framework of DWD and MPI-M: description of the non-hydrostatic dynamical core. *Quarterly Journal of the Royal Meteorological Society*, 141(687), 563–579.

Zhang, F., Bei, N., Rotunno, R., Snyder, C. & Epifanio, C.C. (2007) Mesoscale predictability of moist baroclinic waves: convection-permitting experiments and multistage error growth dynamics. *Journal of the Atmospheric Sciences*, 64(10), 3579–3594. Available from: https://doi.org/10.1175/jas4028.1

Zhang, F., Sun, Y.Q., Magnusson, L., Buizza, R., Lin, S.J., Chen, J.H. et al. (2019) What is the predictability limit of midlatitude weather? *Journal of the Atmospheric Sciences*, 76(4), 1077–1091. Available from: https://doi.org/10.1175/JAS-D-18-0269.1

How to cite this article: Groot, E. & Riemer, M. (2025) When tiny convective spread affects a midlatitude jet: Spread sequence. *Quarterly Journal of the Royal Meteorological Society*, e70049. Available from: https://doi.org/10.1002/qj.70049

APPENDIX A. RELATION JET STREAM SPREAD AND PRECIPITATION RATE SPREAD

We can assume that correlation between upper tropospheric divergence variability and (downstream) PV perturbations is caused by differential divergence, which results from differences in column latent heating. If this is true, the correlation signals found in Section 4.3 can also be diagnosed in an ensemble sensitivity analysis with respect to precipitation rates. This is strongly suggested by the findings of Baumgart *et al.* (2019); Groot and Tost (2023b), and Groot *et al.* (2024).

An ensemble sensitivity analysis of the instantaneous precipitation rate over the Baltic Sea system complements the sensitivity analysis of the mass divergence rate, because upper tropospheric divergence rate is expected to relate linearly to precipitation rate variability across the ensemble—for our case and configuration, see Groot *et al.* (2024). Therefore, we can test implicitly whether box-averaged latent heating perturbations trigger differential divergent outflow winds, which later cause differential advection of PV perturbations further downstream and modify the PV field.

Figure A.1 shows the ensemble sensitivity of 250 hPa PV to precipitation rate variability of the Baltic Sea system at +35 to +38 hr. This is the time interval displaying the strongest downstream correlation about 15–20 hr later, near the PV gradient. Furthermore, the system strongly develops after 35 hr. An elongated feature with of a negative PV perturbation just north of 60°N is visible in Figure A.1 (see also Figure 8f). This feature grows into a larger scale wave-like perturbation at 54 hr, with elongated bands of positive PV perturbations with zonal orientation to the west and east of the dominant PV perturbation, which is negative.

The signal confirms the hypothetical relation between variation in the latent heating and downstream PV perturbations at 250 hPa. Divergent outflows are a key mediator during a cascade of underlying spread-growth processes (Section 4.3). Given the linear correlation R^2 of about 0.8 between mass divergence variability of the Baltic Sea system and its precipitation rate variability within the ensemble (not shown), the signal of Figures 8f and 9 is only slightly diluted in Figure A.1. In short, our statistical analysis of the Baltic Sea system demonstrates that mass divergence is occasionally an important mediator in the evolution of flow spread, which linearly projects latent heating variability (through differential advection) onto the flow further downstream.

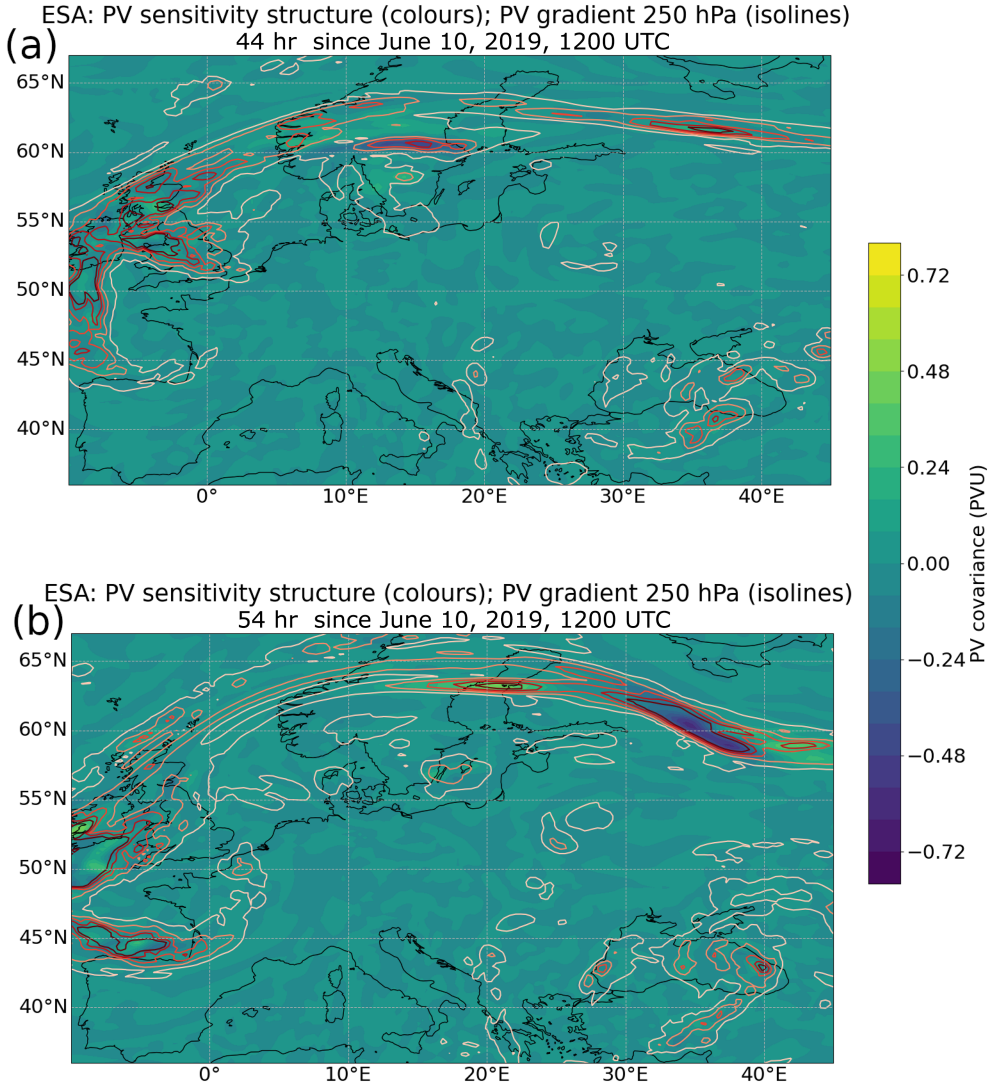

FIGURE A.1 Ensemble sensitivity of the potential vorticity (PV) at 250 hPa with respect to the precipitation rate of the Baltic Sea convective system at 35–38 hr: (a) +44 hr; (b) +54 hr. Isolines indicate the magnitude of PV spread at 250 hPa at 0.16 PVU intervals. ESA: ensemble sensitivity analysis. [Colour figure can be viewed at wileyonlinelibrary.com]